M A S T E R ' S T H E S I S

Numerical simulations of the load bearing behavior of cross-laminated timber

at

Institut für Mechanik der Werkstoffe und Strukturen
Technischen Universität Wien
Fakultät für Bauingenieurwesen

and

Instytut Technologii Informatycznych w Inżynierii Lądowej
Politechnika Krakowska
Wydział Inżynierii Lądowej

Univ. Prof. Dipl.-Ing. Dr. techn. Josef Eberhardsteiner
Dipl.-Ing. Dr. techn. Karin Hofstetter
Dipl.-Ing. Dr. techn. Andreas Jäger
(Institut für Mechanik der Werkstoffe und Strukturen, TU Wien)

Ao. Univ. Prof. Dipl.-Ing. Dr. techn. Jerzy Pamin
(Instytut Technologii Informatycznych w Inżynierii Lądowej, PK)

the author

Bartosz Radecki-Pawlik
Na Wrzosach 45
30-819 Kraków, Poland

October 2009 .....

Acknowledgements

I would like to express my gratitude to all of those who gave me the possibility to complete this thesis. First of all I would like to thank the Institute for Mechanics of Materials and Structures at the Vienna University of Technology. I owe my deepest gratitude to my supervisors: Univ.-Prof. Dipl.-Ing. Dr. techn. Josef Eberhardsteiner, Dipl.-Ing. Dr. techn. Karin Hofstetter and Dipl.-Ing. Dr.techn. Andreas Jäger. I would like to show my gratitude to the Institute for Computational Civil Engineering at the Cracow University of Technology. I am deeply indebted to my supervisor Univ.-Prof. Dipl.-Ing. Dr. techn. Jerzy Pamin.

I would like to thank all of my colleagues from Institute for Mechanics of Materials and Structures. They have made available their support in a number of ways.

Also I would like to thank my family for supporting me and encouraging me, during my stay in Vienna.

I am indebted to many of my friends and colleagues from Cracow and Vienna to support me during writing my thesis, especially those who helped me with accommodation at the last days of my stay in Vienna.

Abstract

In the framework of presented thesis the two-step MCLT (Model for Cross Laminated Timber) is described. The main motivation for this thesis was to develop a simulation tool for investigation of the mechanical behaviour of cross-laminated timber and to apply it to studying the influence of varying mechanical characteristics of the individual lamellae on the overall plate behaviour. As the base for the MCLT one of the already existing two dimensional models - the KAREM model - is chosen. The first programme (simulation programme) generates the stiffness and strength values of each individual lamella of the plate, considering the material parameters, such as lengths of boards, density, knots and moisture content and their variations. A plate with homogeneous mechanical properties is defined as reference plate. The second programme - finite element programme - computes the distributions of deflections, stresses and strains in the framework of elastic and elastic-plastic calculations. The results of computations performed for the reference plate, using the MCLT in the elastic range are compared with analytical results and show a good agreement. The MCLT can be used for estimating the stiffness and the elastic limit load of the plate. The elastic limit is determined for the reference plate and for one hundred plates with randomly distributed material properties. A considerable variation of this limit is observed.

Considering the results of computations using MCLT, it is observed that the plasticisation and the lamination of layers affects the distribution of displacements, stresses and strains. Also the variability of material parameters in the random plates influences the stiffness and elastic limit of the cross-laminated timber.

Contents

Chapter 1

Introduction

1.1 Motivation

The main motivation for this thesis was to develop a simulation load for investigation of the mechanical behaviour of cross-laminated timber and to apply it to studying the influence of varying mechanical characteristics of the individual lamellae on the overall plate behaviour. The cross-laminated timber, which nowadays is more and more used, is wide spreading in all divisions of civil engineering. Not only beams and lattice construction are made of timer, but the folded plate structures.

In the framework of this thesis a two-step model is presented (Model for Cross-Laminated Timber 'MCLT'), which is based on a one-dimensional model for glued laminated timber (KAREM - Karlsruhe model). The first part of the MCLT is the simulation programme. The tasks of this programme are to build up the plate according to its geometry using so-called endless lamellae, and to assign stiffness and strength parameters to each lamella section. Those are determinated from randomly distributed material parameters such as density, moisture content, knot content, and location of finger-joints. Second part of the model is a finite elemente programme, which computes deflections, stresses and strains of the generated plate. The numerical calculations are location of elastic and elastic-plastic.

1.2 Structure of thesis

In the second chapter some general information about laminated timber is provided. In Section 2.1 the principal use of glulam constructions is reviewed. The next Section 2.2 presents a literature survey of existing two-dimensional (2D) and three-dimensional (2D) models for

laminated timber.

The third chapter contains the theoretical background of the presented thesis. In the first section of this chapter (Section 3.1) the principal material directions and the corresponding co-ordinate system of wood are presented. Section 3.2 depicts the mechanical behaviour of wood in framework of elasticity theory and in Section 3.3 of plasticity theory.

In Chapter 4 the two dimensional KAREM model for glulam constructions is presented. Some basic informations about this model are written in Section 4.1. The first step of this model - simulation programme - is described in Section 4.2 and Section 4.3, where material parameters are discussed. Stiffness parameters and strength values for the KAREM model are presented in Section 4.4. Finally the idea of finite elemente calculations is depicted in Section 4.5.

The Chapter 5 treats the Model for Cross-Laminated Timber (MCLT). After the basic concept of MCLT, which is outlined in Section 5.1, the two-step model is presented. The results of the simulation programme, which are described in Sections 5.2 and 5.3 and are calculated using regression equations (Section 5.4), are discussed in Section 5.5. The second-step programme - finite elemente programme - is discussed in Section 5.6.

All of the results computed by means of the MCLT are depicted in Chapter 6. In Section 6.1 the results for the reference plate are discussed, where also a comparison of the numerical results with corresponding exact analytic calculations is made. The results of random plate computations are presented in Section 6.2, where also the histogram of elastic limits for one hundred random plates is presented.

In the last chapter the thesis is summarized and conclusions are drawn.

Chapter 2

Glued laminated timber

2.1 Glulam constructions

One of the most important construction materials of civil engineering, close to concrete and steel, is wood. Because of its natural genesis, wood material parameters are variable. The idea of developing the glued laminated timber was to overcome natural influences, such as knots, pitch pockets or cork inclusions. According to glulam production process, every board is screened. Each "weak part" - including e.g. knots - is cut out. Clear wood parts are joined together using finger-joints. Quasi endless lamellae are built. Finally, gluing laminates with each other, glulam beams are made.

There are several advantages of using glued laminated timber instead of solid wood:

- Using clear wood which is graded
- Higher load carrying capacity allows to use bigger spans
- Using variable cross-sectional shapes
- Curved beams can be formed

It is also worth mentioning that costs of glulam production are comparable with different kinds of material. Nowadays glulam is used for building bridges, sports halls, swimming pools, churches and production halls (see Figure 2.1).

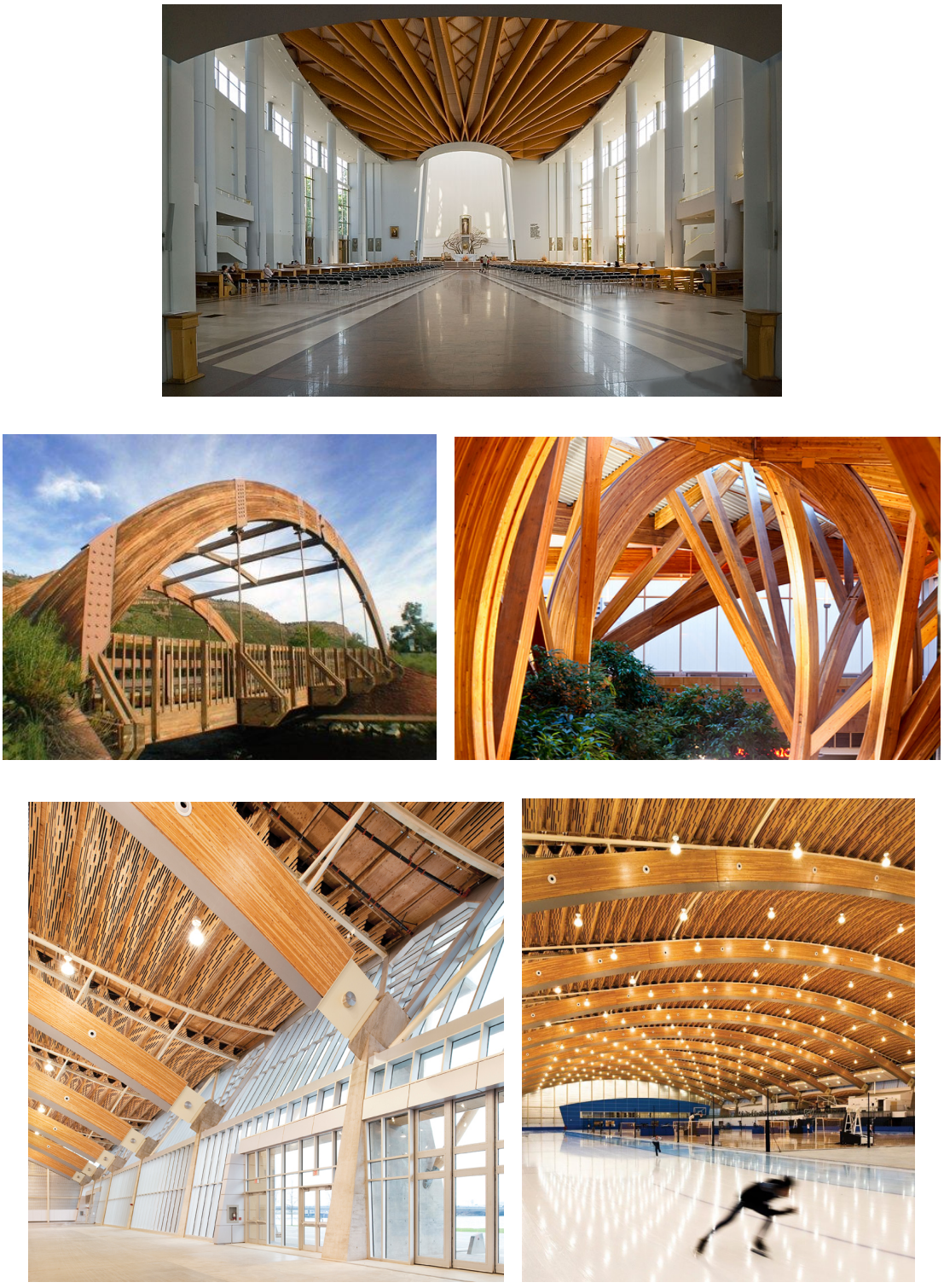

Figure 2.1: Glulam constructions (photos found in www)

2.2 Glulam models

In this section a review of simulation models for glulam is presented.

2.2.1 Two-dimensional (2D) models

The first attempts of calculating timber wood constructions started in the second half of the 20th century. It is possible to divide the existing models into three groups.

1. Empirical I_k/I_g models
   - WILSON AND COTTINGHAM (1947) [30]
   - FREAS AND SELBO (1954) [15]
2. Finite Element models
   - FOSCHI AND BARRETT (1980) [14]
   - EHLBECK ET AL. (1985) [10], [11] AND [12]
   - COLLING (1990) [6], [7] AND [8]
   - GOVINDARAJOO (1989) [17]
   - KLINE ET AL. (1986) [19]
   - BURK AND BENDER (1989) [5]
3. Transformed section models
   - MOODY (1974) [23] AND (1977) [24]
   - BROWN AND SUDDARTH (1977) [3]
   - BENDER ET AL. (1985) [1]
   - RICHBURG (1988) [27]
   - TAYLOR (1988) [29]
   - BURK (1988) [4]

Empirical I_k/I_g models

In the empirical I_k/I_g models, especially the influence of knots on strength is taken into account. I_k - the moment of inertia of knots with diameters smaller than 15 cm - is compared with I_g - the moment of inertia of the whole cross-section of the beam. The acceptable level of maximum stresses, at bending the beam is the result of multiplication of I_k/I_g ratio and the related value of stresses for clear wood.

Finite Element models

The computation and simulation models for glulam are based on the statistical distributions of strength values and stiffnesses of the single glulam lamella. The very first model was developed by FOSCHI AND BARRETT [14]. In 1985 EHLBECK ET AL. [10], [11] and [12] enhanced the FOSCHI AND BARRETT model, where variable lengths of boards, density, knots and constant moisture content are taken into consideration. This model is chosen as the basis for developing the three-dimensional Model for Cross-Laminated Timber (MCLT), which is described in this thesis.

Transformed section models

The transformed section method is used to calculate the bending strength of a beam made of different materials with different elastic moduli E_i. One modulus is chosen as reference modulus, and the dimensions of sections with different moduli are scaled according to the ratio between this modulus and the reference one.

2.2.2 Three-dimensional (3D) models

Existing three-dimensional models of computing the CLT plates are based on three methods:

1. Model based on classical laminate theory
2. γ - Method
3. Shear analogy method.

They are not considered in this work.

Chapter 3

Theoretical background

In this chapter some basic definitions for better comprehensibility of the presented model are defined. Also the mechanical behaviour of wood in the framework of elasticity theory and plasticity theory is depicted.

3.1 Definitions

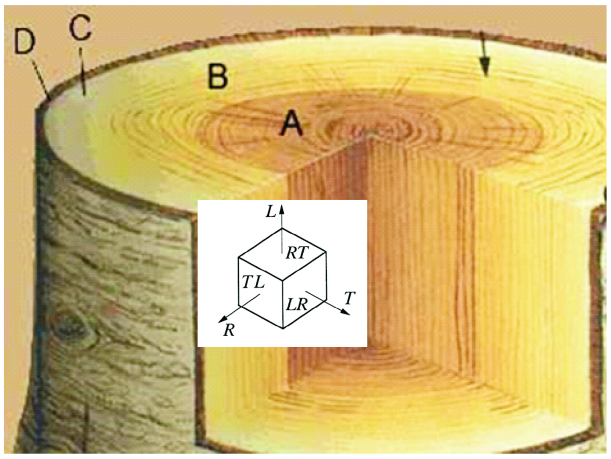

Figure 3.1: A cross-section of wood; co-ordinate system

A log consists of several parts which are depicted in Figure 3.1: A - heartwood; B - sapwood; C - phloem; D - bark. The principal material directions and the corresponding co-ordinate system of wood are strictly connected with the direction of wood fibres and the local orientations

of the annual rings (see Figure 3.1): $L(2)$ - longitudinal (parallel to fibres); $R(3)$ - radial (perpendicular to growth rings); $T(1)$ - transversal (tangential to growth rings).

3.2 Elasticity

Within the framework of continuum mechanics wood is treated as homogeneous material. The mechanical behaviour of timber is generally described in the framework of elasticity theory by means of generalized Hooke's law [18], [20]. In terms of differential components, the respective relation between stresses and strains reads:

$$d\sigma_{ij} = C_{ijkl} d\varepsilon_{kl} \, . \tag{3.1}$$

Let us make an assumption that wood is a material with elastic potential $C_{ijkl} = C_{klij}$ and that σ_{ij} (stress tensor), ε_{ij} (strain tensor) and C_{ijkl} (stiffness tensor) are symmetric. From the symmetry of the stress tensor $\sigma_{ij} = \sigma_{ji}$ it follows that $C_{ijkl} = C_{jikl}$, and from the symmetry of the strain tensor $\varepsilon_{ij} = \varepsilon_{ji}$ that $C_{ijkl} = C_{ijlk}$. Assuming orthotropic nature of wood, the inverse Hooke's law can be written in relation to the principal material directions as:

$$\begin{Bmatrix} d\varepsilon_L \\ d\varepsilon_R \\ d\varepsilon_T \\ d\gamma_{LR} \\ d\gamma_{RT} \\ d\gamma_{TL} \end{Bmatrix} = \begin{bmatrix} \frac{1}{E_L} & -\frac{\nu_{RL}}{E_R} & -\frac{\nu_{TL}}{E_T} & 0 & 0 & 0 \\ -\frac{\nu_{LR}}{E_L} & \frac{1}{E_R} & -\frac{\nu_{TR}}{E_T} & 0 & 0 & 0 \\ -\frac{\nu_{LT}}{E_L} & -\frac{\nu_{RT}}{E_R} & \frac{1}{E_T} & 0 & 0 & 0 \\ 0 & 0 & 0 & \frac{1}{G_{LR}} & 0 & 0 \\ 0 & 0 & 0 & 0 & \frac{1}{G_{RT}} & 0 \\ 0 & 0 & 0 & 0 & 0 & \frac{1}{G_{TL}} \end{bmatrix} \begin{Bmatrix} d\sigma_L \\ d\sigma_R \\ d\sigma_T \\ d\tau_{LR} \\ d\tau_{RT} \\ d\tau_{TL} \end{Bmatrix} . \tag{3.2}$$

With symmetry conditions we have:

$$\frac{\nu_{LR}}{E_L} = \frac{\nu_{RL}}{E_R}, \frac{\nu_{RT}}{E_R} = \frac{\nu_{TR}}{E_T}, \frac{\nu_{TL}}{E_T} = \frac{\nu_{LT}}{E_L} \, . \tag{3.3}$$

Therein nine independent material constants of wood - elasticity moduli E_L, E_R, E_T, shear moduli G_{LR}, G_{RT}, G_{TL} and Poisson ratios $\nu_{LR}, \nu_{RT}, \nu_{TL}$ are used. For uniaxial straining of a beam in longitudinal direction, equations 3.2 are reduced to:

$$d\varepsilon_L = \frac{1}{E_L} \cdot \sigma_L \, . \tag{3.4}$$

3.3 Plasticity

The Tsai-Wu failure criterion suitably describes the onset of failure in orthotropic materials. The mathematical equation of the failure surface reads as:

$$f(\sigma_{ij}) = a_{ij}\sigma_{ij} + b_{ijkl}\sigma_{ij}\sigma_{kl} - 1 \qquad i,j,k,l = 1,2,3 \, , \tag{3.5}$$

where the tensors a_{ij}, b_{ijkl} contain the information about the orthotropic material parameters, and σ_{ij} denotes the components of the stress tensor. Formulating the failure criterion in relation to the principal material directions L, R and T results in:

$$\begin{aligned} f = & a_{LL}\sigma_{LL} + a_{RR}\sigma_{RR} + a_{TT}\sigma_{TT} \\ & + b_{LLLL}\sigma_{LL}^2 + b_{RRRR}\sigma_{RR}^2 + b_{TTTT}\sigma_{TT}^2 \\ & + 2 \cdot b_{LLRR}\sigma_{LL}\sigma_{RR} + 2 \cdot b_{RRTT}\sigma_{RR}\sigma_{TT} + 2 \cdot b_{TTLL}\sigma_{TT}\sigma_{LL} \\ & + 4 \cdot b_{LRLR}\tau_{LR}^2 + 4 \cdot b_{RTRT}\tau_{RT}^2 + 4 \cdot b_{TLTL}\tau_{TL}^2 \\ & - 1 \end{aligned} \quad , \tag{3.6}$$

with 12 independent Tsai-Wu parameters. Nine of these parameters can be defined in terms of uniaxial strengths and shear strengths as:

$$\begin{aligned} a_{LL} &= \frac{1}{\left|f_{y_{t_L}}^k\right|} - \frac{1}{\left|f_{y_{c_L}}^k\right|} \\ b_{LLLL} &= \frac{1}{\left|f_{y_{t_L}}^k\right| \cdot \left|f_{y_{c_L}}^k\right|} \\ a_{RR} &= \frac{1}{\left|f_{y_{t_R}}^k\right|} - \frac{1}{\left|f_{y_{c_R}}^k\right|} \\ b_{RRRR} &= \frac{1}{\left|f_{y_{t_R}}^k\right| \cdot \left|f_{y_{c_R}}^k\right|} \\ a_{TT} &= \frac{1}{\left|f_{y_{t_T}}^k\right|} - \frac{1}{\left|f_{y_{c_T}}^k\right|} \\ b_{TTTT} &= \frac{1}{\left|f_{y_{t_T}}^k\right| \cdot \left|f_{y_{c_T}}^k\right|} \\ b_{LRLR} &= \frac{1}{4 \cdot \left(f_{y_{LR}}^k\right)^2} \\ b_{RTRT} &= \frac{1}{4 \cdot \left(f_{y_{RT}}^k\right)^2} \\ b_{TLTL} &= \frac{1}{4 \cdot \left(f_{y_{TL}}^k\right)^2} \end{aligned} \quad , \tag{3.7}$$

where $f_{y_{t_L}}^k$, $f_{y_{t_R}}^k$, $f_{y_{t_T}}^k$ devote uniaxial strength values for tension, $f_{y_{c_L}}^k$, $f_{y_{c_R}}^k$, $f_{y_{c_T}}^k$ uniaxial strength values for compression, and $f_{y_{LR}}^k$, $f_{y_{RT}}^k$, $f_{y_{TL}}^k$ - shear strength values.

The remaining three Tsai-Wu parameters can only be obtained from biaxial tests. They are taken as zero values in the following calculations:

$$\begin{aligned} b_{LLRR} &= 0 \\ b_{RRTT} &= 0 \\ b_{TTLL} &= 0 \end{aligned} \quad . \tag{3.8}$$

The Return-Mapping algorithm is used for the numerical solution of the elastic-plastic problem in the framework of the FE calculations [28].

Chapter 4

KAREM - Karlsruhe Rechenmodell

The two dimensional model KAREM (Karlsruhe Rechenmodell) for glulam timber is presented in this chapter. This model is chosen as the basis method for developing the three dimensional Model for Cross-Laminated Timber.

4.1 The basic concept

In 1985, on the basis of an already established model for the mechanical behaviour of timber beams [14], a new computational model was developed [10][11][12].

Ehlbeck et al. [10] write about the KAREM model:
"A computer model was developed to predict the load-carrying capacity of glulam beams. This model includes two computer programmes. The first one simulates the built-up beam taking into account the wood density and the knots of the boards as well as the finger joints. The stiffness and strength values of the lamellae are calculated for each section by using regression equations. The second programme predicts the load-carrying capacity of the beams using a finite element method, taking into account a redistribution of forces when single sections fail, and the non-linear stress-strain relationship of wood under compression."

In the framework of this thesis the first programme is so-called "simulation programme" and the second programme "finite elemente programme".

4.2 Simulation programme

The first task of the simulation program is to build up the glulam beam. The program generates endless lamellae (see Figure 4.1), which consist of boards connected by finger-joints. The total length of the lamellae is determined by the sum of lengths of boards.

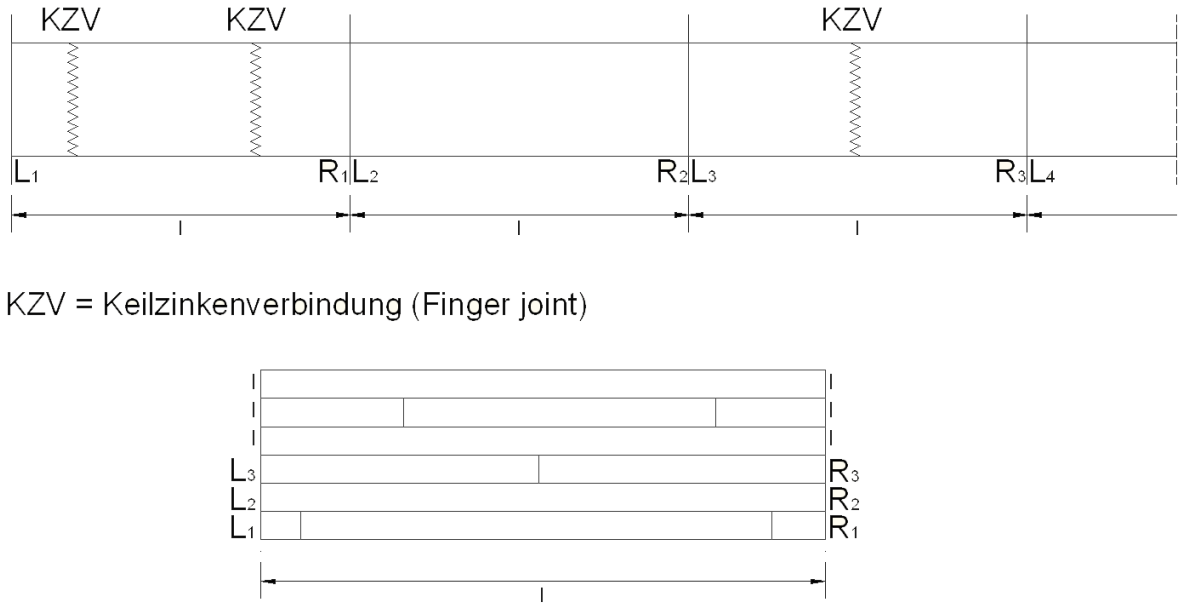

Figure 4.1: Idea of building up a glulam beam with an endless lamella (l - the length of the glulam beam)

Every board is divided into singular cells (sections), which have a length of 150 mm each (see Figure 4.2). According to DIN 4074 and the ECE-laws, the size of the cell is strictly connected with the definition of the knot size parameter (Knot Area Ratio - value - see Chapter 4.3.4), which is also evaluated for board sections of 150 mm length. Using statistical distributions of

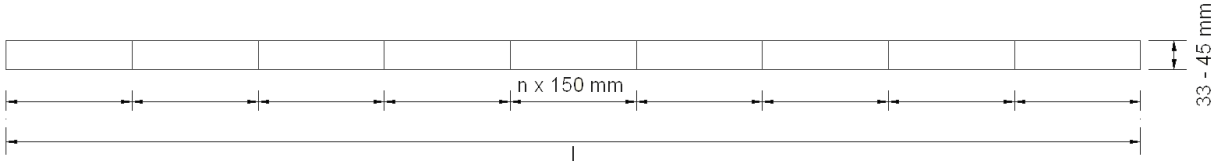

Figure 4.2: Partitioning of a board into singular cells of 150 mm length

parameters - such as density, knot area ratio (KAR-value), moisture content and location of finger joints - every cell is assigned random values of these parameters. Finally, the last step of the simulation program is to calculate the stiffness and strength values for every cell based on these parameters by means of regression equations. Also a mean value of the distributed stiffness over all cells is calculated as control value.

4.3 Input parameters - simulation programme

4.3.1 Geometry of glulam beam

Two parameters - the length and the height - define the geometrical properties of the glulam beam. It should be mentioned that the width, as the third dimension, is omitted because of the two-dimensional (2D) approach. The height of each board has to be in the range between 33 and 45 mm in order to stay within the limits set by the regression equations (see Chapter 4.4). It is chosen together with the number of boards in order to reach the height of the beam (see Figures 4.1, 4.2).

4.3.2 Finger joints - lengths of boards

Lengths of boards are variable and are determined by the technology of producing glulam. Originally the distribution of board lengths in the KAREM simulation programme [10][11][12] was set according to Larsen [22]. In the evolution of KAREM model, a new distribution function for the board lengths was developed [2]. According to Blaß et al. [2] it is possible to distinguish two production modes: some companies produce mainly long boards, others mainly short boards. The distribution of an arbitrary combination of boards of these two groups, can be presented as the sum of two normal distributions - with quotient 50% to 50%. The first distribution with mean value $\mu = 4.62$ m and standard deviation $\sigma = 0.67$ m represents the first production mode making long boards; whereas the second one, with mean value $\mu = 2.15$ m and standard deviation $\sigma = 0.50$ m, represents the second production mode making short boards (see Figure 4.3).

4.3.3 Density

Glos [16] describes the typical distribution of densities in a batch of timber boards by a normal distribution with mean value $\mu = 0.43$ g/cm^3 and standard deviation $\sigma = 0.05$ g/cm^3 (see Figure 4.4). This distribution is used in the simulation programme. Ehlbeck et al. investigated the density difference between the two ends of a board for 111 boards. They found out that for more than 80% this difference is below 0.04 g/cm^3. Hence, a constant density value can be assigned to all cells of a specific board.

4.3.4 Knot Area Ratio (KAR-value)

The influence of knots on a clear wood cell is estimated by the Knot Area Ratio (KAR-value), which relates the sum of the cross-sectional area of the knots at a cross-section to the cross-sectional area of the cell (see Figure 4.5). The length of a cell is typically 150 mm as mentioned before.

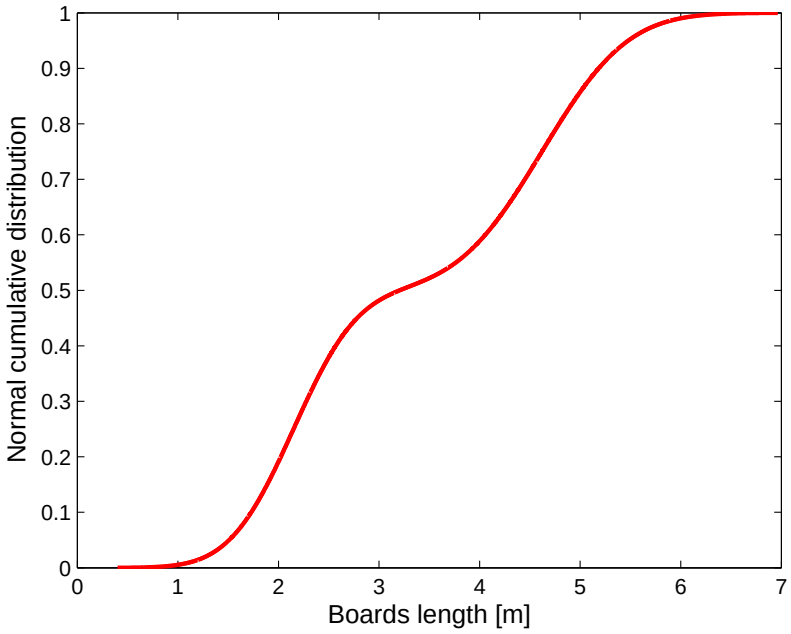

Figure 4.3: The sum of two normal cumulative distributions of board lengths [m]

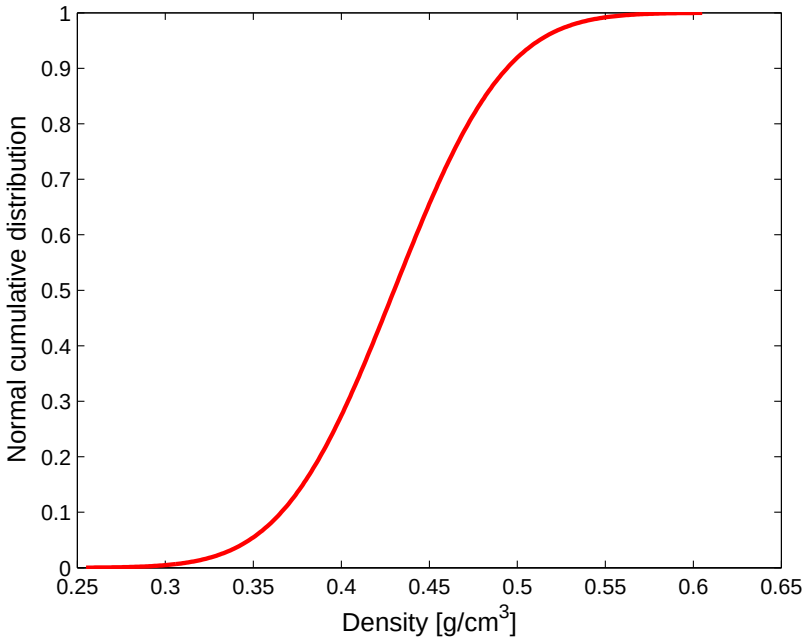

Figure 4.4: Normal cumulative distribution of density [g/cm^3]

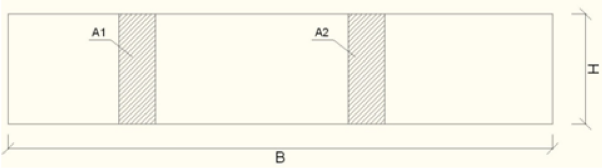

Figure 4.5: Definition of KAR-value; $KAR = (A1 + A2)/(B \cdot H)$

Ehlbeck et al. [11] investigated the frequency of occurrence of various KAR-values in boards of different quality classes. The results are depicted in Figure 4.6. Finally KAR-values are assigned to each cell based upon these probability distributions of actual knot occurrences in graded lumber.

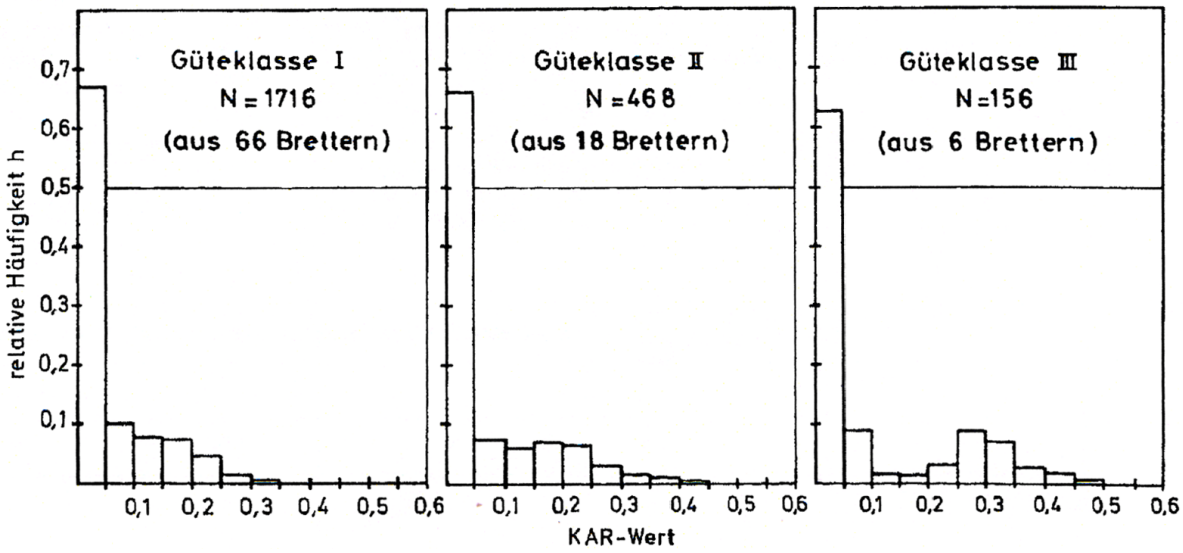

Figure 4.6: Frequency distribution of a certain KAR-value in a 150 mm long board section, related to different visual grade classes ('Güteklasse I-III') according to DIN 4074 [11]

4.3.5 Moisture content

According to Ehlbeck et al. [11], a constant moisture content of $u = 12\ \%$ is chosen for the whole beam.

4.4 Regression equations

As soon as input parameters are known, it is possible to use regression equations to calculate stiffness and strength values for every cell of endless lamellae depending on these parameters.

In general, such as equation read as:

$$\ln(Y) = a_1 X_1 + b_1 X_2 + c_1 + S_1(0; s_1) \ , \tag{4.1}$$

where Y describes the dependent variable (e.g. tension stiffness), X_1 and X_2 are independent input variables (e.g. density, KAR-value), and a_1, b_1, c_1 specify constant values determined from experiments. S_1 is the residue of the analytic function $\ln(Y)$, which shows a normal distribution with mean value $\mu = 0$ and standard deviation $\sigma = s_1$.

For endless lamellae cells without finger joints, the elastic moduli in longitudinal compression and tension, E_c^k and E_t^k, as well as the strengths, $f_{y_c}^k$ and $f_{y_t}^k$, can be approximated in terms of density ρ_0, moisture constant u and KAR-value as:

$$\begin{aligned}
\ln\left(E_c^k\right) &= 8.22 + 3.19 \cdot \rho_0 - 0.602 \cdot KAR - 13.6 \cdot \rho_0 \cdot u^2 - 11.0 \cdot KAR \cdot u^2 \\
&\qquad \mu = 0.142,\ \sigma = 0.80 \\
\ln\left(f_{y_c}^k\right) &= 3.23 + 2.8 \cdot \rho_0 - 0.825 \cdot KAR - 5.37 \cdot u \\
&\qquad \mu = 0.088,\ \sigma = 0.94 \\
\ln\left(E_t^k\right) &= 8.2 + 3.13 \cdot \rho_0 - 1.17 \cdot KAR \\
&\qquad \mu = 0.180,\ \sigma = 0.77 \\
\ln\left(f_{y_t}^k\right) &= -4.22 + 0.876 \cdot \ln\left(E_t^k\right) - 0.093 \cdot KAR \cdot \ln\left(E_t^k\right) \\
&\qquad \mu = 0.187,\ \sigma = 0.86
\end{aligned} \ , \tag{4.2}$$

where μ is the mean value of the residue, and σ its standard deviation.

These equations are used by Glos and Ehlbeck et al. [11], the regression equations (Eq. 4.2) and (Eq. 4.3) to predict the mechanical properties of 150 mm long board sections.

For endless lamellae cells including finger joints, the corresponding equations read as:

$$\begin{aligned}
\ln\left(E_c^{k^{KZV}}\right) &= 8.43 + 2.53 \cdot \rho_0 - 10.3 \cdot u^2 \\
&\qquad \mu = 0.231,\ \sigma = 0.56 \\
\ln\left(f_{y_c}^{k^{KZV}}\right) &= -3.05 + 0.816 \cdot \ln\left(E_c^{k^{KZV}}\right) + 68.4 \cdot \rho_0 \cdot u - 1.3 \cdot u^2 \cdot \ln\left(E_c^{k^{KZV}}\right) \\
&\qquad \mu = 0.116,\ \sigma = 0.92 \\
\ln\left(E_t^{k^{KZV}}\right) &= 8.459 + 2.517 \cdot \rho_0 \\
&\qquad \mu = 0.142,\ \sigma = 0.61 \\
\ln\left(f_{y_t}^{k^{KZV}}\right) &= 2.716 + 5.905 \cdot 10^{-5} \cdot E_t^{k^{KZV}} \\
&\qquad \mu = 0.231,\ \sigma = 0.52
\end{aligned} \ . \tag{4.3}$$

All of the presented regression equations are valid for boards showing heights in the range between 33 and 45 mm.

To verify the correctness of the computed stiffness, the average lamellae stiffness is calculated from the stiffness values assigned to the individual cells assuming a series connection:

$$E_{sim} = \frac{n}{\sum\limits_{i=1}^{n} \frac{1}{E_i}} \ , \tag{4.4}$$

where E_i describes the stiffness of each cell i, and n is the number of cells. If the simulation stiffness is within a tolerance interval specified according to experimental data for glulam beam stiffnesses, the simulation is finished; otherwise, the simulation has to be repeated.

4.5 Finite element program

As soon as the geometry of the glulam beam is known, every lamella section has its material parameters (depending on local board length, density, KAR-value and moisture content), and every lamella has its section moduli of elasticity and strength values. The boundary conditions and loading have to be defined. Using the finite element method (FEM), where the mesh size is corresponding to the size of the lamellae cell, stresses in every lamella section are determined. As long as the stress values in all lamella sections are smaller than the corresponding strength values, the load is linearly increased. If the compression strength is reached in a certain cell, the compression strength is assigned to the particular cell as the constant stress value. Otherwise, if the tension strength in a certain cell is reached, the cell is excluded from further calculation with the stress value equal to zero.

Chapter 5

Model for Cross-Laminated Timber

5.1 The basic concept

Using the main components of KAREM model (simulation program and FEM program), a three-dimensional Model for Cross-Laminated Timber (MCLT) is developed. A square plate model is built up with the simulation program. As a result of this, Young's moduli (E_L, E_R, E_T), shear moduli (G_{LR}, G_{RT}, G_{TL}), Poisson's ratios (ν_{LR}, ν_{RT}, ν_{TL}) as well as strength values (uniaxial strengths f_{y_L}, f_{y_R}, f_{y_T} both for tension and for compression and shear strengths $f_{y_{LR}}$, $f_{y_{RT}}$, $f_{y_{TL}}$) for glulam lamellae cells with and without knots are determined from density, moisture content, and KAR-value. The second program, using the FEM, predicts the limit of elasticity for each cross-laminated timber plate.

5.2 Simulation programme

The task of the simulation programme is to build up the plate. Randomly distributed material parameters such as density, moisture content, knots and finger-joints are assigned to the individual cell lamellae. By means of regression equations, the stiffness and strength values of these cells are computed there from.

Two kinds of plates are simulated: a reference plate - in which every cell of the lamellae has the same, average values of material parameters; and a so-called random plate - where every cell of the lamellae is assigned random values of material parameters. This will be detailed in the following subsections.

5.3 Input parameters - simulation program

In analogy to the KAREM model, input parameters for the simulation program must first be determined.

5.3.1 Geometry of cross-laminated timber plate

A three-layer square plate was chosen for calculations. The plate dimensions are shown in Figure 5.1. Both the reference plate and the random plate have the same geometry.

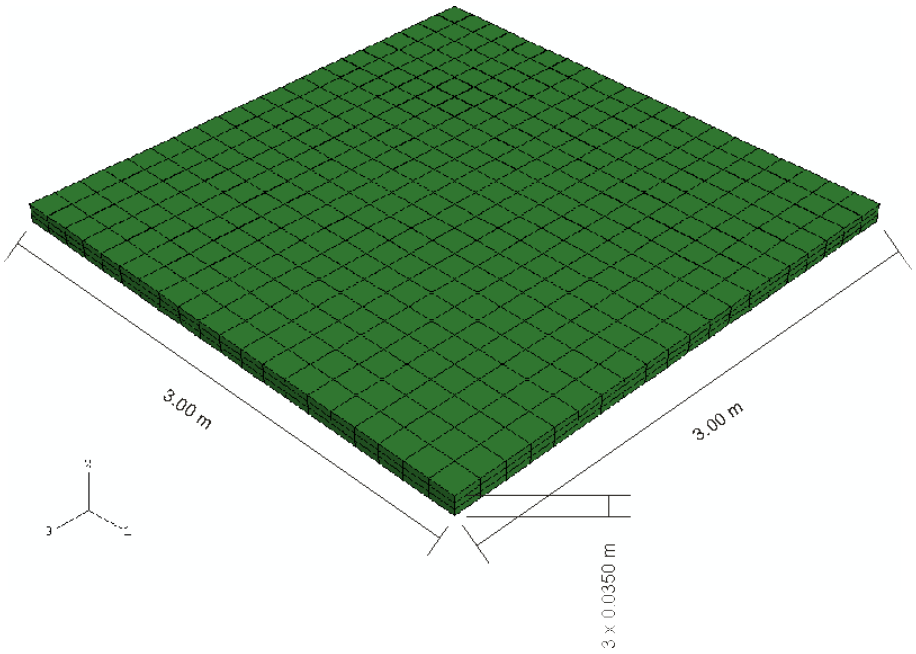

Figure 5.1: Dimensions of investigated CLT plate and assigned co-ordinate system

According to the KAREM model, every layer of the plate is built up of endless lamellae, where the longitudinal directions of wood fibres correspond to the global directions of the co-ordinate system: odd layers - axis 1 (see Figure 5.2); even layers - axis 3 (see Figure 5.3).

Like in the KAREM model, every lamella is built up of boards, whereas every board is divided into cells with square shape in the plate plane (sections), each having dimensions 150 mm length and 35 mm height (see Figure 5.4).

5.3.2 Random plate

In the random plate, the input parameters adopted in subsequent sections are randomly assigned to every single cell of the glulam lamellae.

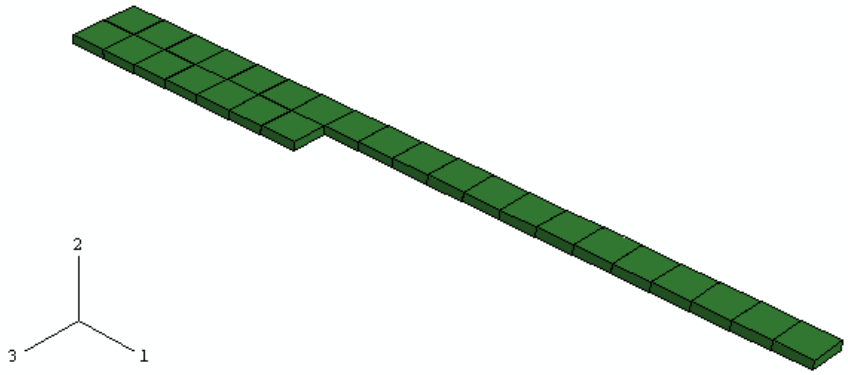

Figure 5.2: Orientation of longitudinal direction of wood fibres - odd layers - parallel to axis 1

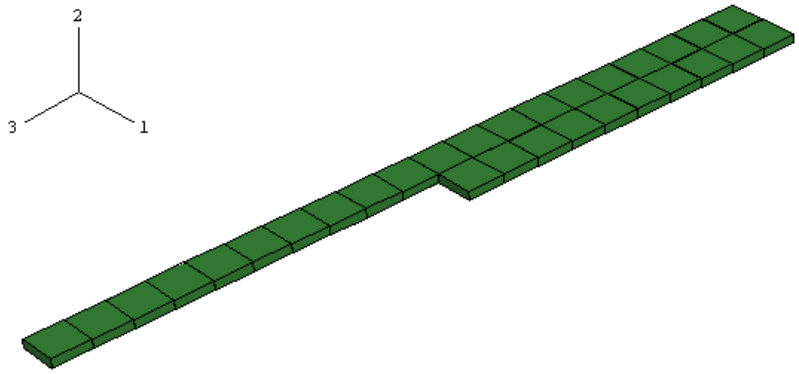

Figure 5.3: Orientation of longitudinal direction of wood fibres - even layers - parallel to axis 3

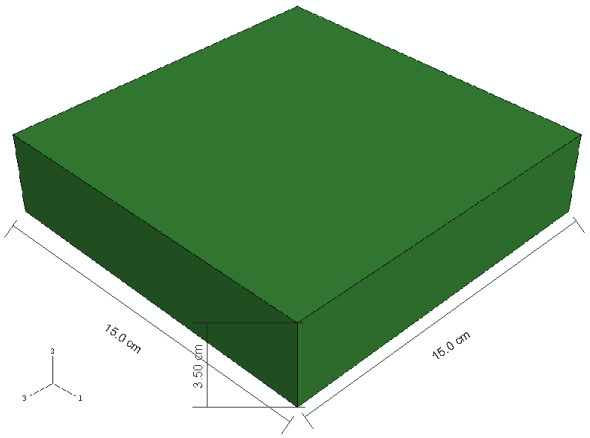

Figure 5.4: Dimensions of plate unit cell (side length $l = 150$ [mm]; thickness $h = 35$ [mm])

5.3.2.1 Finger joints - lengths of boards

A random values of the board length are chosen from the board length distribution - which is the same as in the KAREM model (see Figure 4.3). It is assumed that the boards are connected by finger joints in order to produce the endless lamellae. Thus, the board lengths control the distances of the finger joints.

5.3.2.2 Density

A constant density value is assigned to every cell in each board. The board density is chosen randomly based on the density distribution (see Figure 4.4) specified in the KAREM model. Every board is attributed a random density.

5.3.2.3 Knot Area Ratio (KAR-value)

The frequency distribution of KAR-values in a 150 mm long board section, related to the visual grade class II of wood (see Figure 4.6), is approximated by a Weibull distribution function (see Figure 5.5).

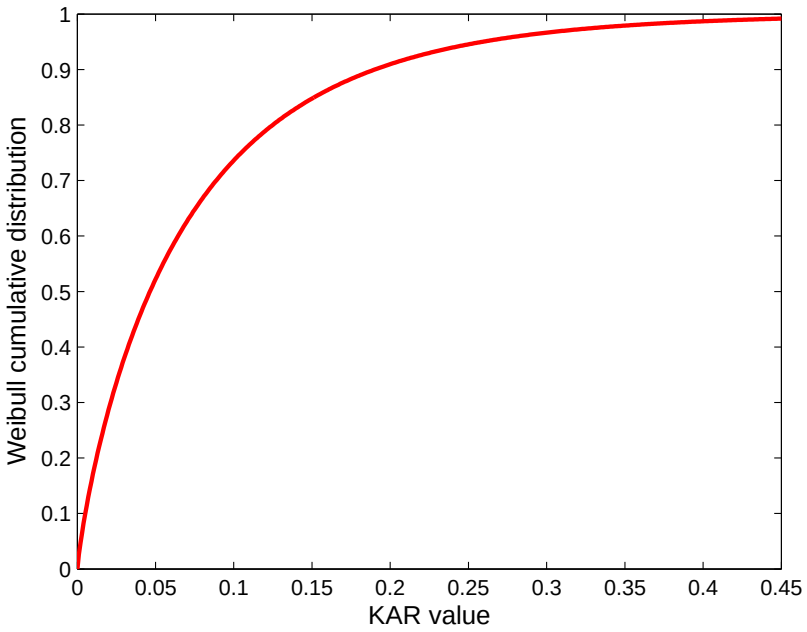

Figure 5.5: Weibull cumulative distribution of KAR-values [-]

A randomly chosen KAR-value from the Weibull distribution (see Figure 5.5) is assigned to every single cell of the lamellae.

5.3.2.4 Moisture content

According to standard ambient conditions and air humidity, a constant moisture content of $u = 12\ \%$ is chosen for the whole board.

5.3.3 Reference plate

In the reference plate, no finger joints in the endless lamellae are assumed. A constant value of every input parameter is assigned to every single cell of the lamellae, namely:

$$\begin{aligned} &\rho = 0.430\,[g/cm^3] \\ &KAR = 0.0475 \\ &u = 12\ \% \end{aligned} \quad . \tag{5.1}$$

5.4 Regression equations

The influence of the input parameters (density, moisture contents and KAR-value) on the mechanical parameters is considered in terms of regression equations, which are presented in the following sections.

5.4.1 Elasticity moduli and Poisson's Ratios

The following regression equations are defined on the basis of a micromechanical model reference:

$$\begin{aligned} E_L &= 9221 \cdot (0.0099 \cdot \rho^2 + 2.2171 \cdot \rho + 0.0003) \cdot (0.3586 \cdot u^2 - 1.4994 \cdot u + 1.2853) \\ E_R &= 474 \cdot (8.8179 \cdot \rho^2 - 2.4399 \cdot \rho + 0.3067) \cdot (1.4053 \cdot u^2 - 6.0702 \cdot u + 2.1586) \\ E_T &= 319 \cdot (8.7603 \cdot \rho^2 - 2.0279 \cdot \rho + 0.1377) \cdot (1.5297 \cdot u^2 - 6.2122 \cdot u + 2.1822) \\ G_{LR} &= 587 \cdot (0.7135 \cdot \rho^2 + 1.8226 \cdot \rho + 0.0351) \cdot (0.3576 \cdot u^2 - 2.4174 \cdot u + 1.4697) \\ G_{RT} &= 34 \cdot (21.8869 \cdot \rho^2 - 12.0464 \cdot \rho + 1.9763) \cdot (1.7218 \cdot u^2 - 6.4270 \cdot u + 2.2176) \\ G_{TL} &= 576 \cdot (0.7135 \cdot \rho^2 + 1.8226 \cdot \rho + 0.0351) \cdot (0.3576 \cdot u^2 - 2.4174 \cdot u + 1.4697) \\ \nu_{LR} &= 0.3314 \cdot (-0.3026 \cdot \rho^2 - 0.7715 \cdot \rho + 1.4086) \cdot (-5.6132 \cdot u^2 + 1.8779 \cdot u + 0.8380) \\ \nu_{RT} &= 0.7305 \cdot (3.4835 \cdot \rho^2 - 4.7469 \cdot \rho + 2.4319) \cdot (1.6248 \cdot u^2 + 0.2281 \cdot u + 0.8902) \\ \nu_{TL} &= 0.0128 \cdot (-2.2411 \cdot \rho^2 + 4.9597 \cdot \rho - 0.7771) \cdot (-9.4366 \cdot u^2 - 0.2391 \cdot u + 1.4210) \end{aligned} \quad . \tag{5.2}$$

These equations are sensitive to specified units, which are (g/cm^3 for density and N/mm^2 for the elasticity moduli). The functions (Eq. 5.2) describing the influence of density and moisture content on the elastic constants of wood are formulated for clear wood, i.e. knots are not taken into account.

In order to consider the influence of knots on the nine elastic constants, an additional approximate reduction ratio is defined. For this purpose, the knot is approximated by a circular

cylinder with its axis in R-direction. The dimensions and according directions are specified in Figure 5.6.

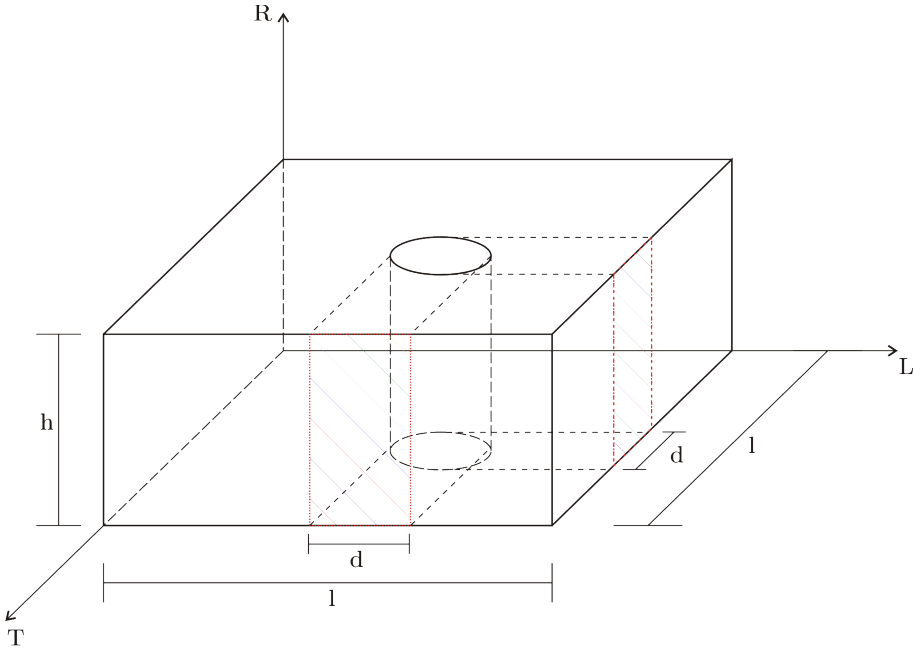

Figure 5.6: Representative knot - dimensions

Two kinds of reduction ratios are defined - a linear reduction ratio and a quadratic one:

$$\begin{aligned} k_l &= \tfrac{l-d}{l} \\ k_q &= \tfrac{l^2-\pi\frac{d^2}{4}}{l^2} \end{aligned} \quad . \tag{5.3}$$

Using the definition of the KAR-value (see Figure 4.5) the reduction ratios can be written as follows:

$$\begin{aligned} k_l &= 1 - KAR \\ k_q &= 1 - \pi \cdot \tfrac{(KAR)^2}{4} \end{aligned} \quad . \tag{5.4}$$

In terms of the reduction ratios, the moduli of elasticity are reduced as follows:

$$\begin{aligned} E_L^k &= k_l \cdot E_L \\ E_R^k &= k_q \cdot E_R \\ E_T^k &= k_l \cdot E_T \\ G_{LR}^k &= k_l \cdot G_{LR} \\ G_{RT}^k &= k_l \cdot G_{RT} \\ G_{TL}^k &= k_l \cdot G_{TL} \end{aligned} \quad . \tag{5.5}$$

For the Poisson's ratios the following relations are used:

$$\frac{\nu_{ij}^k}{E_j^k} = \frac{\nu_{ji}^k}{E_i^k} \, , \tag{5.6}$$

where an assumption is made that ν^k_{LR}, ν^k_{RT} and ν^k_{TL} are not affected by knots. So the remaining Poisson's ratios, according to Eq. (5.6), read as:

$$\begin{aligned} \nu^k_{RL} &= \frac{E^k_L \nu^k_{LR}}{E^k_R} \\ \nu^k_{LT} &= \frac{E^k_T \nu^k_{TL}}{E^k_L} \\ \nu^k_{TR} &= \frac{E^k_R \nu^k_{RT}}{E^k_T} \end{aligned} \quad . \tag{5.7}$$

As for the reference plate the elastic constants every endless lamella cell has the following material parameters:

$$\begin{aligned} E^k_{L,ref} &= 9319.80\,[N/mm^2] \\ E^k_{R,ref} &= 609.40\,[N/mm^2] \\ E^k_{T,ref} &= 392.50\,[N/mm^2] \\ G^k_{LR,ref} &= 629.80\,[N/mm^2] \\ G^k_{RT,ref} &= 40.20\,[N/mm^2] \\ G^k_{TL,ref} &= 618.00\,[N/mm^2] \\ \nu^k_{LR,ref} &= 0.3324 \\ \nu^k_{TR,ref} &= 0.4581 \\ \nu^k_{TL,ref} &= 0.0151 \end{aligned} \quad . \tag{5.8}$$

5.4.2 Strength values

The influence of density on the strength values (uniaxial strengths f_{y_L}, f_{y_R}, f_{y_T} both for tension and compression as well as shear strengths $f_{y_{LR}}$, $f_{y_{LT}}$, $f_{y_{TR}}$) is again estimated by means of a micromechanical model of wood. Firstly the reference strength values are defined $f^{ref}_{y_{t_L}}$, $f^{ref}_{y_{t_R}}$, $f^{ref}_{y_{t_T}}$ which are strength values for uniaxial tension in longitudinal, radial, and tangential direction; $f^{ref}_{y_{c_L}}$, $f^{ref}_{y_{c_R}}$, $f^{ref}_{y_{c_T}}$ - strength values for uniaxial compression in longitudinal, radial, and tangential direction; $f^{ref}_{y_{LR}}$, $f^{ref}_{y_{LT}}$, $f^{ref}_{y_{TR}}$ - shear strength values, respectively):

$$\begin{aligned} f^{ref}_{y_{t_L}} &= 85.41[N/mm^2]^{*} \\ f^{ref}_{y_{t_R}} &= 2.56[N/mm^2]^{**} \\ f^{ref}_{y_{t_T}} &= 4.23\,[N/mm^2]^{**} \\ f^{ref}_{y_{c_L}} &= 49.98[N/mm^2]^{*} \\ f^{ref}_{y_{c_R}} &= 4.20[N/mm^2]^{**} \\ f^{ref}_{y_{c_T}} &= 5.60\,[N/mm^2]^{**} \\ f^{ref}_{y_{LR}} &= 8.25[N/mm^2]^{*} \\ f^{ref}_{y_{LT}} &= 8.25[N/mm^2]^{*} \\ f^{ref}_{y_{TR}} &= 2.50[N/mm^2]^{***} \end{aligned} \quad . \tag{5.9}$$

where (*) are taken from [9]; (**) from [21];(***) is determined from experiments.

As a result of the micromechanical model of wood, influence functions fs_{ij} of relative strength versus density are obtained (see Figure 5.7). The reference density is set to 0.350 g/cm^3

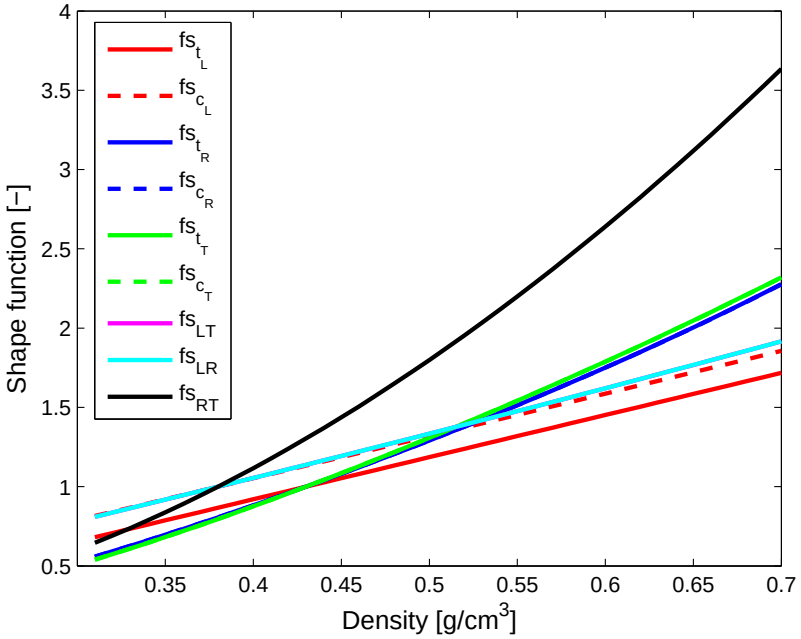

Figure 5.7: Influence functions versus density

or to 0.430 g/cm^3. Finally influence functions are multiplied by the reference strength values (Eq. 5.9), which gives the sought strength values versus density without influence of knots (see Eq. 5.10).

$$\begin{aligned}
f_{y_{t_L}} &= f_{y_{t_L}}^{ref} \cdot fs_L^t(\rho) \\
f_{y_{t_R}} &= f_{y_{t_R}}^{ref} \cdot fs_R^t(\rho) \\
f_{y_{t_T}} &= f_{y_{t_T}}^{ref} \cdot fs_T^t(\rho) \\
f_{y_{c_L}} &= f_{y_{c_L}}^{ref} \cdot fs_L^c(\rho) \\
f_{y_{c_R}} &= f_{y_{c_R}}^{ref} \cdot fs_R^c(\rho) \\
f_{y_{c_T}} &= f_{y_{t_T}}^{ref} \cdot fs_T^c(\rho) \\
f_{y_{LR}} &= f_{y_{LR}}^{ref} \cdot fs_{LR}(\rho) \\
f_{y_{LT}} &= f_{y_{LT}}^{ref} \cdot fs_{LT}(\rho) \\
f_{y_{RT}} &= f_{y_{RT}}^{ref} \cdot fs_{RT}(\rho)
\end{aligned} \quad . \tag{5.10}$$

Again, this set of equations holds for clear, i.e. knot-free wood. The reduction of the uniaxial tensile strengths as a consequence of knots is determined as [13]:

$$\begin{aligned}
f_{y_{t_L}}^k &= f_{y_{t_L}} \cdot e^{-2.78 \cdot KAR} \\
f_{y_{t_R}}^k &= f_{y_{t_R}} \cdot e^{-4.56 \cdot KAR} \\
f_{y_{t_T}}^k &= f_{y_{t_T}} \cdot e^{-4.56 \cdot KAR}
\end{aligned} \quad . \tag{5.11}$$

According to experimental results [13], describing the reduction of the uniaxial compression

strengths in consequence of knots, data are qualitatively specified as follows:

$$\begin{aligned} f^k_{y_{c_L}} &= \frac{f^{k,ex}_{y_{c_L}}}{f^{ex}_{y_{c_L}}} \cdot f_{y_{c_L}} + \left(f_{y_{c_L}} - \frac{f^{k,ex}_{y_{c_L}}}{f^{ex}_{y_{c_L}}} \right) \cdot e^{-rc \cdot KAR} \\ f^k_{y_{c_R}} &= \frac{f^{k,ex}_{y_{c_R}}}{f^{ex}_{y_{c_R}}} \cdot f_{y_{c_R}} + \left(f_{y_{c_R}} - \frac{f^{k,ex}_{y_{c_R}}}{f^{ex}_{y_{c_R}}} \right) \cdot e^{-rc \cdot KAR} \\ f^k_{y_{c_T}} &= \frac{f^{k,ex}_{y_{c_T}}}{f^{ex}_{y_{c_T}}} \cdot f_{y_{c_T}} + \left(f_{y_{c_T}} - \frac{f^{k,ex}_{y_{c_T}}}{f^{ex}_{y_{c_T}}} \right) \cdot e^{-rc \cdot KAR} \end{aligned} \quad , \tag{5.12}$$

where experimental values are specified according to [13]:

$$\begin{aligned} f^{k,ex}_{y_{c_L}} &= 30.50\,[N/mm^2] \\ f^{ex}_{y_{c_L}} &= 46.20\,[N/mm^2] \\ f^{k,ex}_{y_{c_R}} &= 3.48\,[N/mm^2] \\ f^{ex}_{y_{c_R}} &= 5.15\,[N/mm^2] \\ f^{k,ex}_{y_{c_T}} &= 3.48\,[N/mm^2] \\ f^{ex}_{y_{c_T}} &= 5.15\,[N/mm^2] \\ rc &= 50 \end{aligned} \quad . \tag{5.13}$$

As for the shear strengths, considerations based on the Mohr circle are exploited in order to describe the influence of knots. The angle ϕ_{ij} is defined as (see Figure 5.8):

$$\phi_{ij} = \mathrm{tg}^{-1} \frac{2 \cdot f_{y_{ij}}}{f_{y_{t_j}} - f_{y_{c_j}}} \, . \tag{5.14}$$

where $f_{y_{ij}}$, $f_{y_{t_j}}$, $f_{y_{c_j}}$ are clear wood values. Assuming that ϕ_{ij} is constant and not affected by knots, reformulation of Eq. (5.14) with reduced uniaxial strength values for wood with knots results in a similar relation:

$$\phi_{ij} = \mathrm{tg}^{-1} \frac{2 \cdot f^k_{y_{ij}}}{f^k_{y_{t_j}} - f^k_{y_{c_j}}} \, . \tag{5.15}$$

This allows for the calculation of reduced shear strength values as:

$$f^k_{y_{ij}} = \frac{f^k_{y_{t_j}} - f^k_{y_{c_j}}}{2} \, \mathrm{tg}\left(\phi_{ij}\right) \, . \tag{5.16}$$

Specifying Eq. (5.16) for different principal material directions in wood yields:

$$\begin{aligned} f^k_{y_{LR}} &= \frac{f^k_{y_{t_R}} - f^k_{y_{c_R}}}{2} \, \mathrm{tg}\left(\phi_{LR}\right) \\ f^k_{y_{LT}} &= \frac{f^k_{y_{t_T}} - f^k_{y_{c_T}}}{2} \, \mathrm{tg}\left(\phi_{LT}\right) \\ f^k_{y_{RT}} &= \frac{f^k_{y_{t_T}} - f^k_{y_{c_T}}}{2} \, \mathrm{tg}\left(\phi_{RT}\right) \end{aligned} \quad , \tag{5.17}$$

which presents the shear strength values used in the described model.

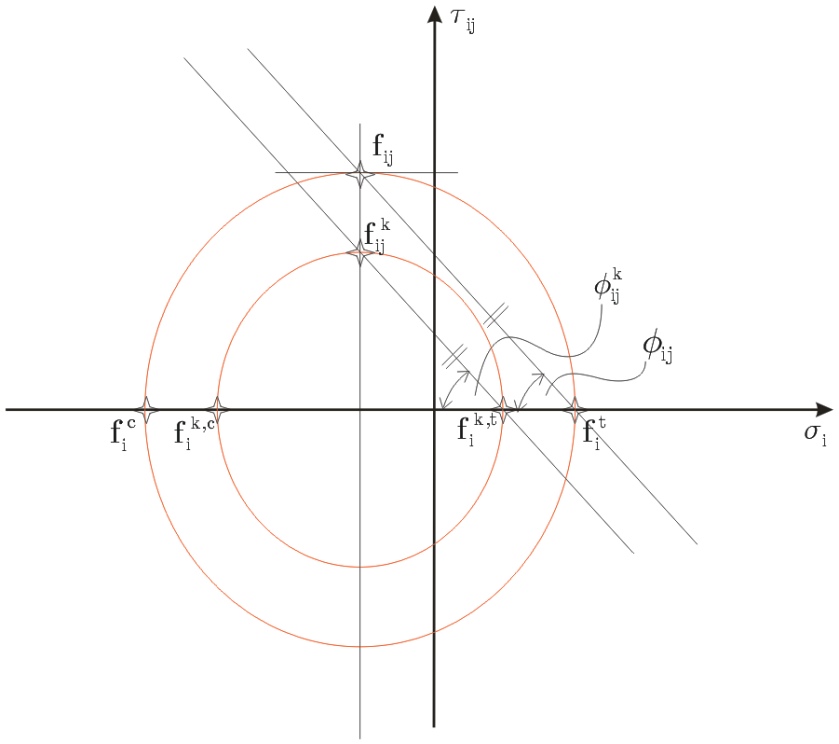

Figure 5.8: Mohr circle - angle $\phi_{ij} = \phi_{ij}^k$

5.5 Study of influence of input parameters on elastic and strength properties

In order to validate the input data and the regression equations, an input parameter study is performed in order to investigate the influences of density and KAR-value on stiffness and strength properties. The correctness of the simulation program is confirmed. Also the realistic range of each parameters is presented.

5.5.1 Influence of density

The influence of density on Young's moduli (E_L^k, E_R^k, E_T^k), shear moduli (G_{LR}^k, G_{RT}^k, G_{TL}^k), Poisson's ratios (ν_{LR}^k, ν_{RT}^k, ν_{TL}^k) and strength values (uniaxial strengths $f_{y_L}^k$, $f_{y_R}^k$, $f_{y_T}^k$ both for tension and for compression as well as shear strengths $f_{y_{LR}}^k$, $f_{y_{RT}}^k$, $f_{y_{TL}}^k$) is studied by evaluating the corresponding equations (Eqs. 5.11, 5.12, 5.17) for a density interval of $\rho \in [\mu - 2\sigma; \mu + 2\sigma]$ and for two selected KAR-values ($KAR = 0$, $KAR = 0.0475$).

5.5.1.1 Elastic properties

Figure 5.9 shows that all elasticity moduli (E_L^k, E_R^k, E_T^k, G_{LR}^k, G_{RT}^k, G_{TL}^k) increase with increasing density.

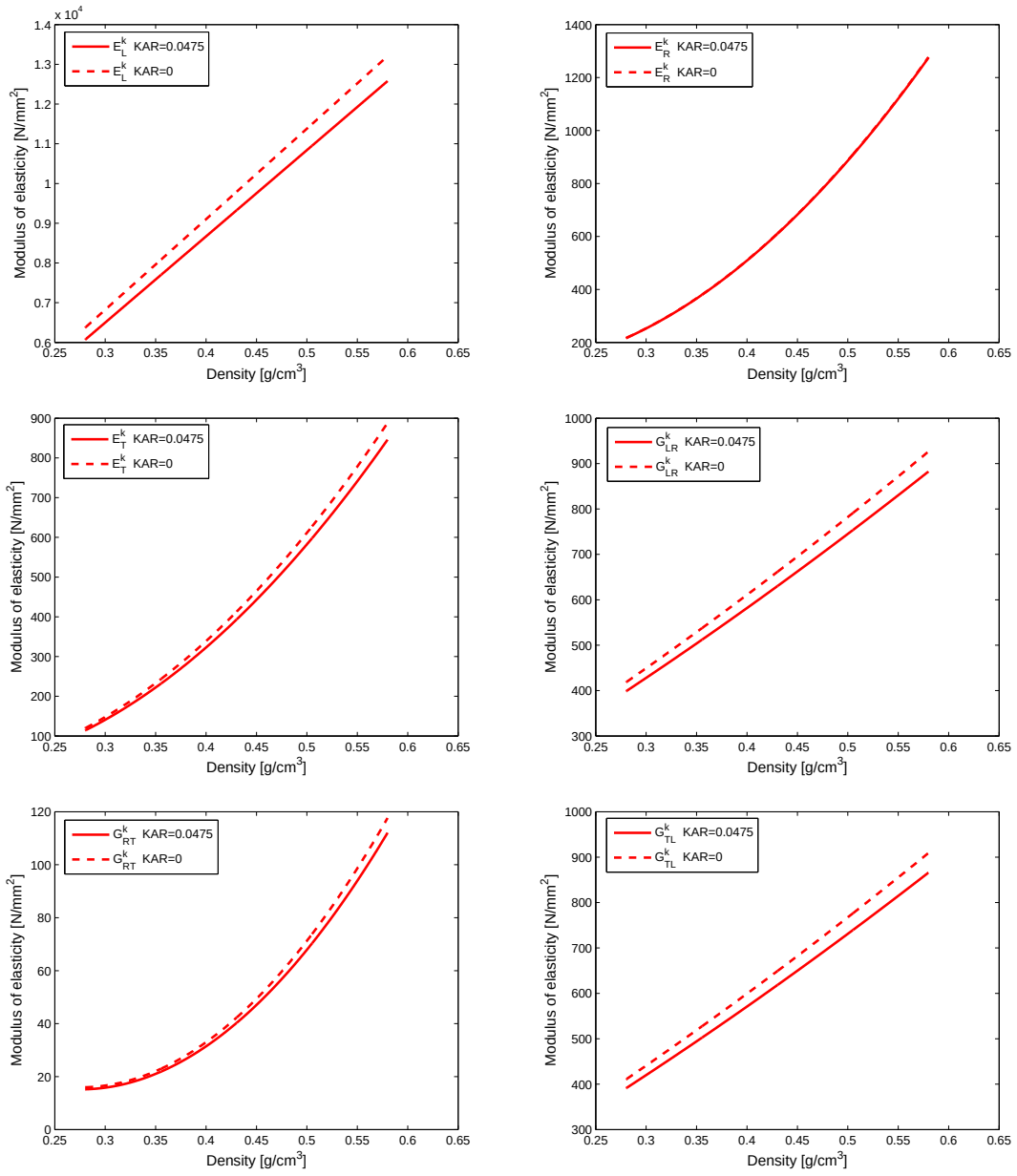

Figure 5.9: Influence of density and KAR-value on Young's moduli according to Eqs. (5.11), (5.12), (5.17)

It is worth mentioning that along with the increase of KAR-value all elasticity moduli decrease (see Figure 5.9). For the selected values $KAR = 0$ and $KAR = 0.0475$, the difference in radial Young's modulus is hardly visible. However, E_R^k decreases with the increase of KAR-value (see following subsection).

Figure 5.10 shows the variation of Poisson's ratios (ν^k_{LT}, ν^k_{RT}, ν^k_{RL}), again for the density interval of $\rho \in [\mu - 2\sigma; \mu + 2\sigma]$ and two different KAR-values ($KAR = 0$, $KAR = 0.0475$).

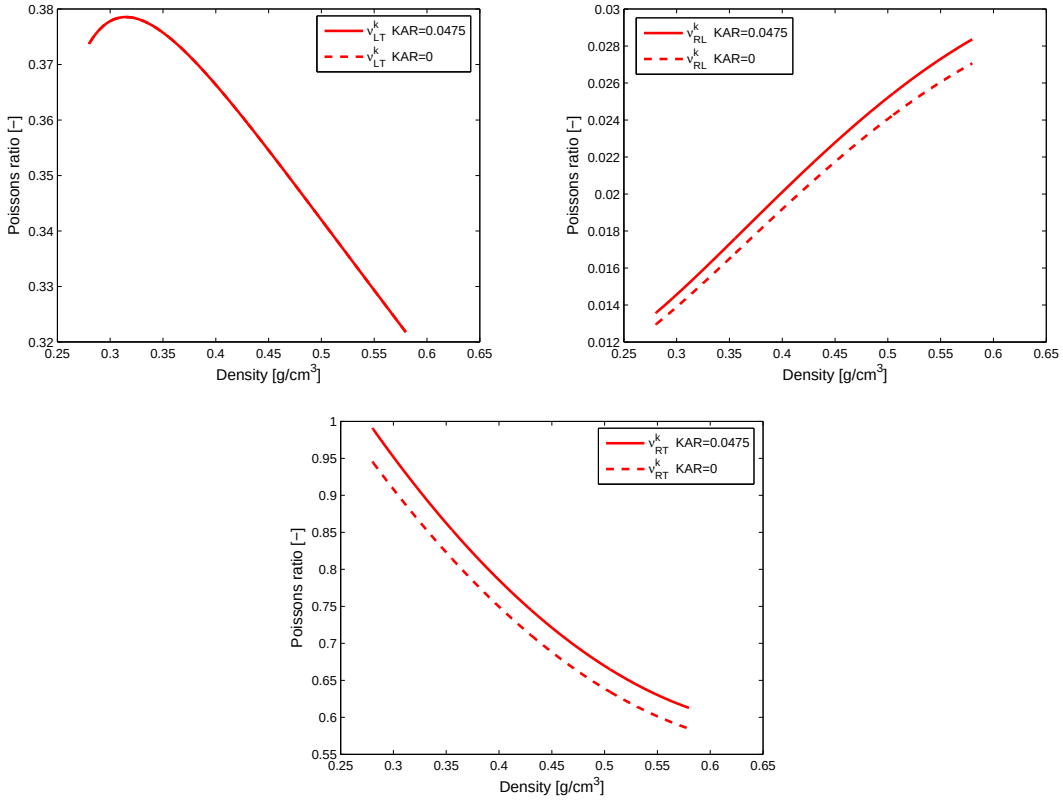

Figure 5.10: Influence of density and KAR-value on Poisson's ratios according to Eq. (5.7)

The influence of density on Poisson's ratios is quite different compared to the elastic moduli, which show a continuous increase with increasing density. The Poisson's ratios ν^k_{LT} and ν^k_{RT} decrease significantly with the increase of density, whereas Poisson's ratio ν^k_{RL} shows an increasing tendency (see Figure 5.10). The Poisson's ratios ν^k_{RT} and ν^k_{RL} increase when the KAR-value grows, whereas the Poisson's ratio ν^k_{LT} seems to be knot-independent. It should be mentioned that the value of a Poisson's ratio is sometimes higher than 0.5 because of the orthotropic material.

5.5.1.2 Strength properties

The influence of density on the strength values for tension ($f^k_{y_{t_L}}$ - longitudinal direction; $f^k_{y_{t_R}}$ - radial direction; $f^k_{y_{t_T}}$ - tangential direction) and compression ($f^k_{y_{c_L}}$ - longitudinal direction; $f^k_{y_{c_R}}$ - radial direction; $f^k_{y_{c_T}}$ - tangential direction) and on shear strengths ($f^k_{y_{LR}}$; $f^k_{y_{LT}}$; $f^k_{y_{TR}}$) is studied. Equations (5.12), (5.13), (5.17) are evaluated for two constant KAR-values ($KAR = 0$, $KAR = 0.0475$) and a density interval of $\rho \in [\mu - 2\sigma; \mu + 2\sigma]$ (see Figure 5.11).

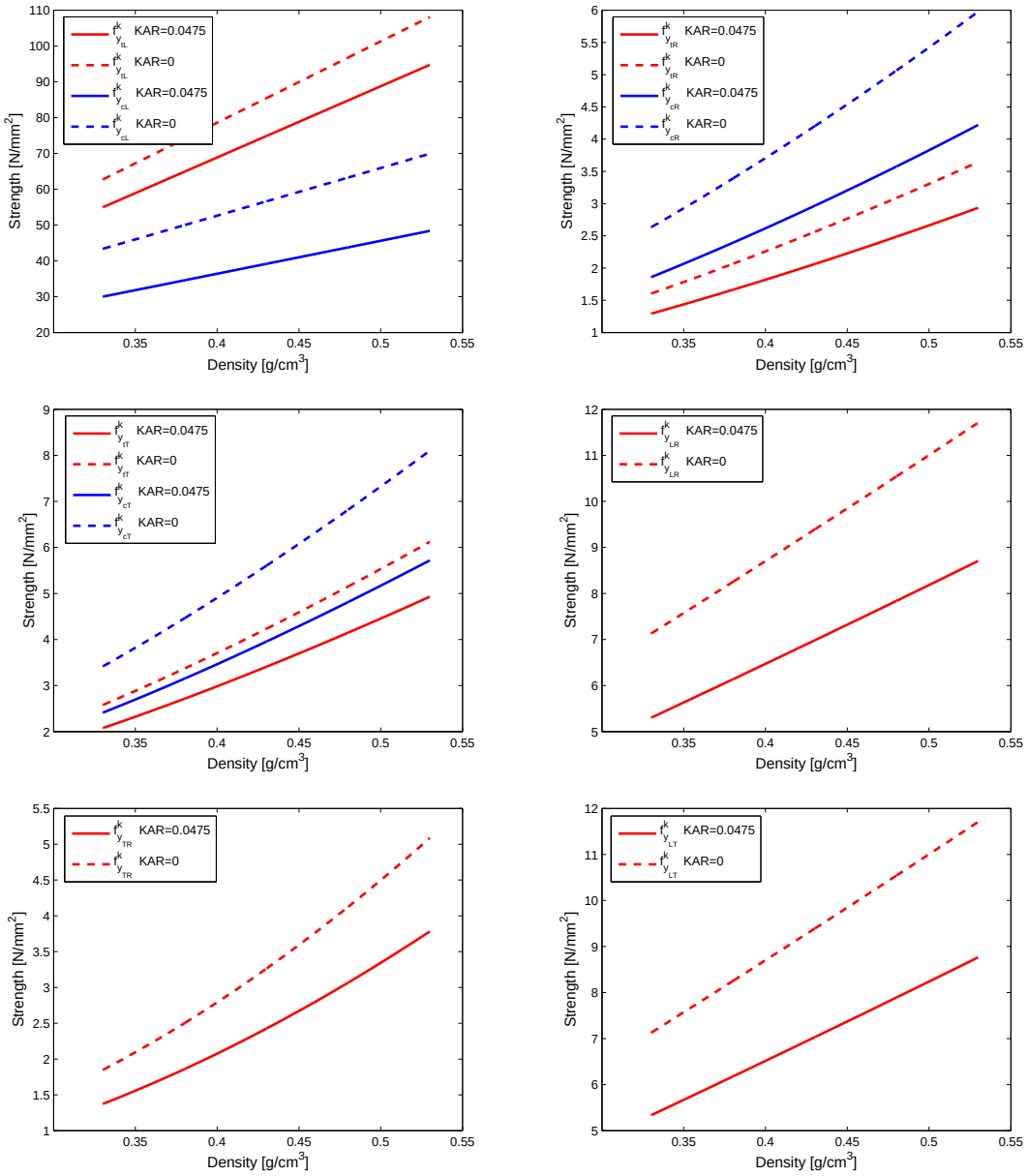

Figure 5.11: Influence of density and KAR-value on strength values according to Eqs. (5.12), (5.13), (5.17)

The strength course in relation to density and knots is quite similar to that of the elasticity moduli. Along with density increase, all of the strength values increase (see Figure 5.11).

5.5.2 Influence of KAR-value

The influence of KAR-value on Young's moduli (E_L^k, E_R^k, E_T^k), shear moduli (G_{LR}^k, G_{RT}^k, G_{TL}^k), Poisson's ratios (ν_{LR}^k, ν_{RT}^k, ν_{TL}^k) and strength values ($f_{y_L}^k$, $f_{y_R}^k$, $f_{y_T}^k$ both for tension and compression as well as shear strengths $f_{y_{LR}}^k$, $f_{y_{RT}}^k$, $f_{y_{TL}}^k$) is studied by evaluating the corresponding Equations (5.11), (5.12), (5.17) for KAR-values in the interval of $[0; 0.5]$ and for chosen density.

5.5.2.1 Elastic properties

The variation of elasticity moduli (E_L^k, E_R^k, E_T^k), and shear moduli G_{LR}^k, G_{RT}^k, G_{TL}^k) with changing KAR-values, for three selected densities ($\rho = \mu - 2 \cdot \sigma$, $\rho = \mu$, $\rho = \mu + 2 \cdot \sigma$) is plotted in Figure 5.12. For all moduli a decreasing tendency with increasing KAR-value is observed.

Figure 5.13 shows the variation of Poisson's ratios (ν_{LT}^k, ν_{RT}^k, ν_{RL}^k) for $KAR \in [0; 0.5]$ and for the mean density ($\rho = \mu$). The analysis shows a different behaviour of each Poisson's ratio for varying density values.

The Poisson's ratios ν_{RL}^k and ν_{RT}^k increase with the increasing KAR-values, whereas Poisson's ratio ν_{LT}^k is constant (see Figure 5.13).

5.5.2.2 Strength properties

The parameter study for the strength values for uniaxial tension ($f_{y_{t_L}}^k$; $f_{y_{t_R}}^k$; $f_{y_{t_T}}^k$), uniaxial compression ($f_{y_{c_L}}^k$; $f_{y_{c_R}}^k$; $f_{y_{c_T}}^k$) and shear ($f_{y_{LR}}^k$; $f_{y_{LT}}^k$; $f_{y_{TR}}^k$) is depicted in Figure 5.14. The corresponding equations are evaluated for three different densities ($\rho = \mu - 2 \cdot \sigma$, $\rho = \mu$, $\rho = \mu + 2 \cdot \sigma$) and for $KAR \in [0; 0.5]$. For all strength parameters a decreasing tendency with increasing KAR-values is observed. It is worth mentioning that according to experiments, the decreasing tendency of compression strength values with increasing KAR-value equal to 0.1 is observed up to KAR-value of 0.1. Above this, the compression strengths are more or less constant.

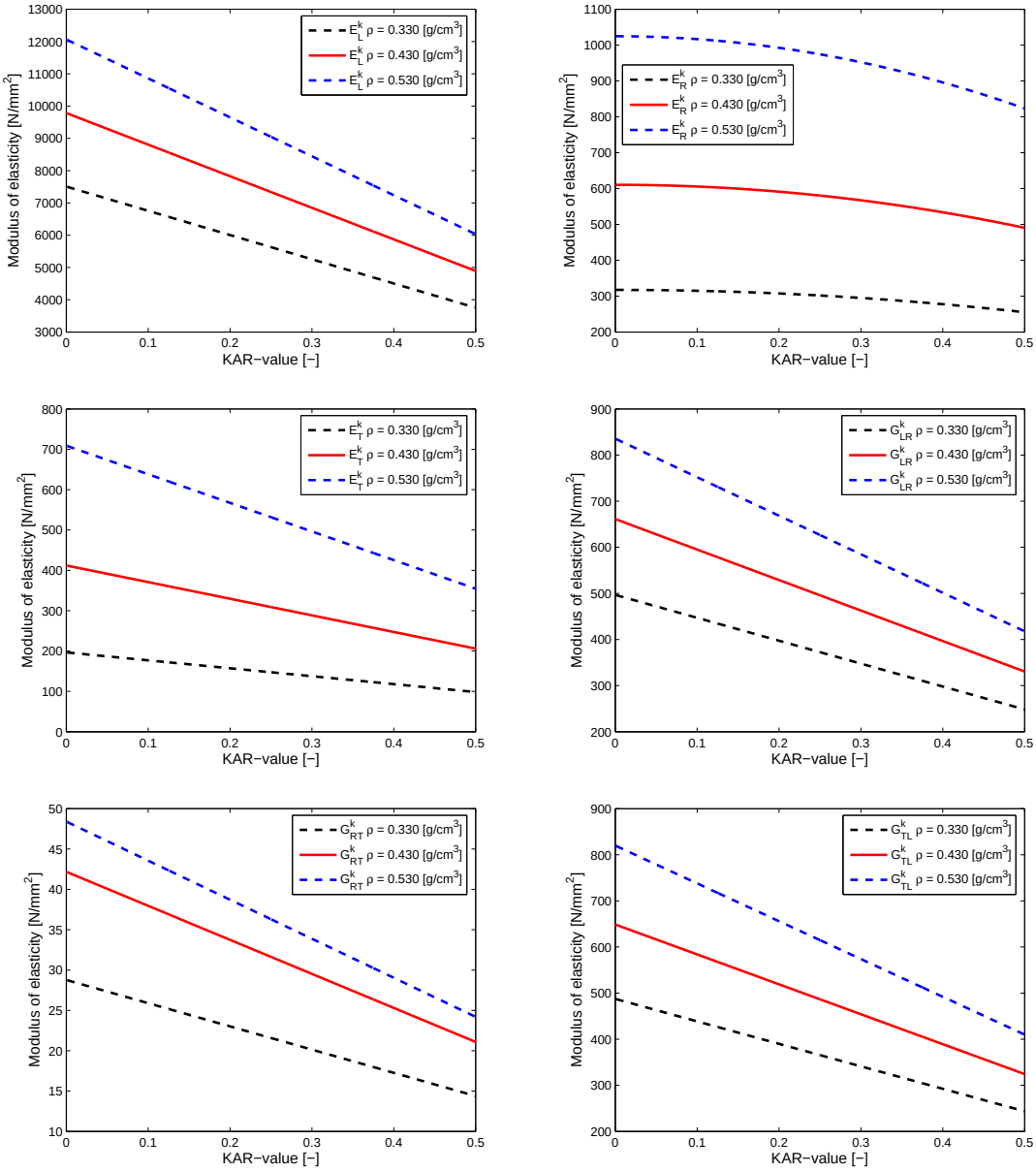

Figure 5.12: Influence of KAR-value and density on Young's moduli according to Eqs. (5.11), (5.12), (5.17)

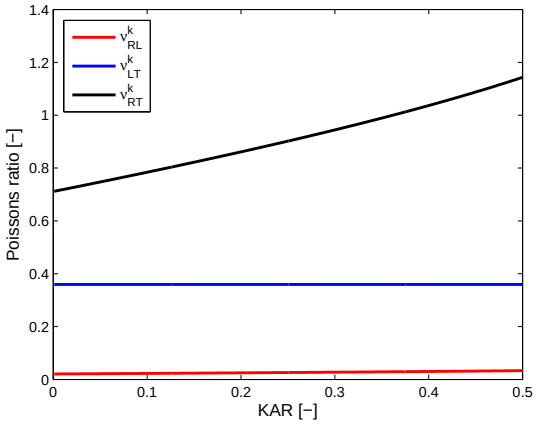

Figure 5.13: Influence of KAR-value and density on Poisson's ratio according to Eq. (5.7)

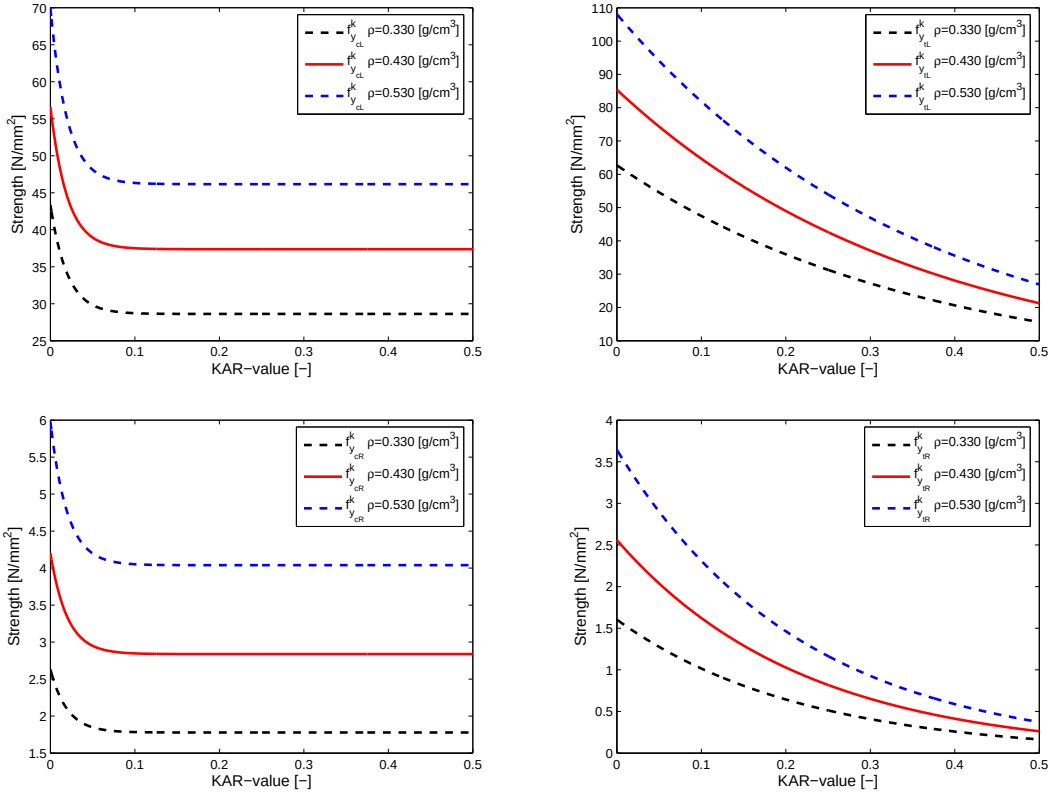

Figure 5.14: Influence of KAR-value and density on strength according to Eqs. (5.12), (5.13), (5.17) - part 1

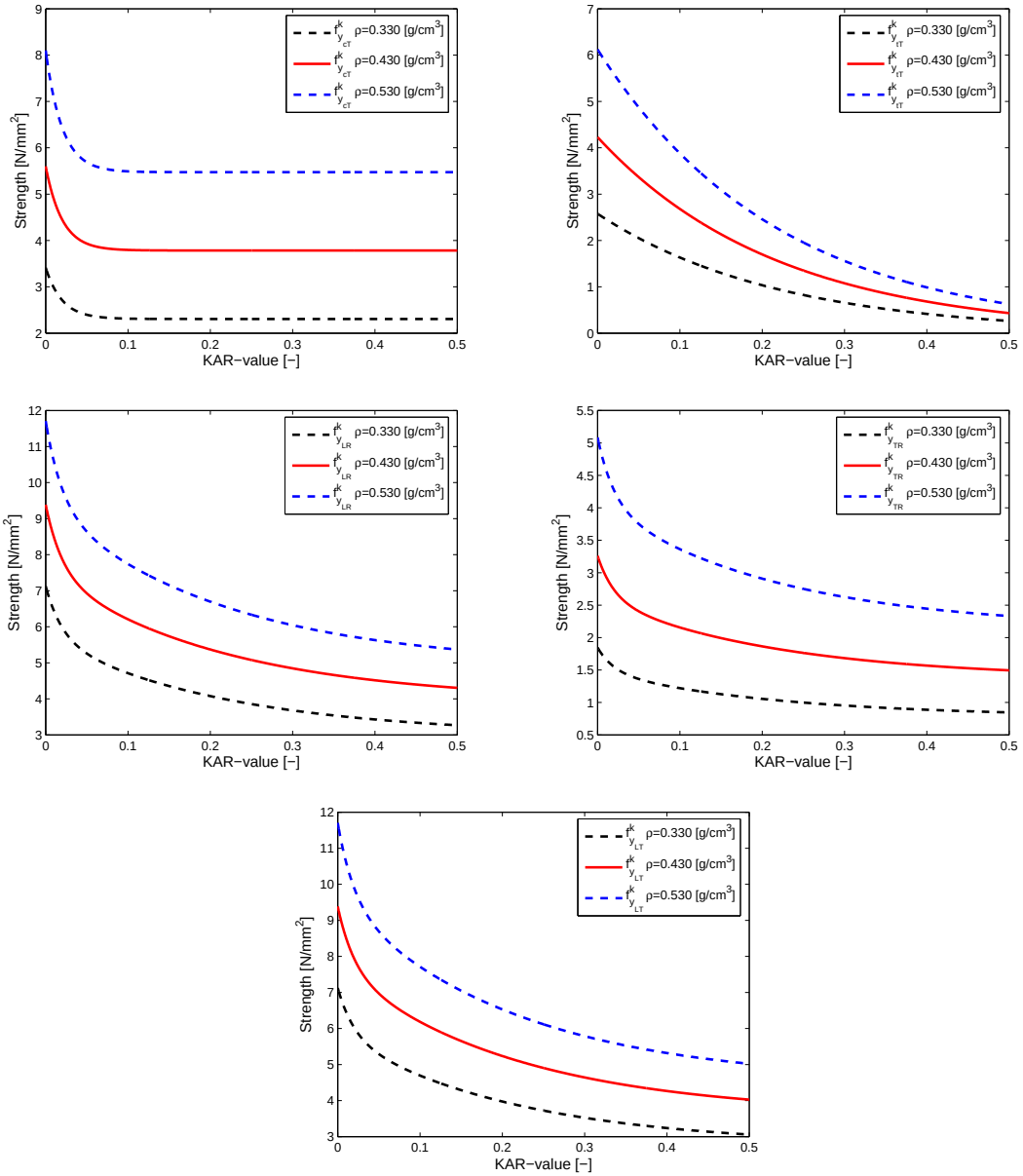

Figure 5.14: Influence of KAR-value and density on strength according to Eqs. (5.12), (5.13), (5.17) - part 2

5.6 FEM - model

In this section the finite elemente model for mechanical calculations of the plate is presented. The FE model is established in order to compute deflections, stresses and strains of CLT timber plates. The commercial FE Software ABAQUS 6.6.2 is used to calculate the simulated cross-laminated timber plates.

5.6.1 Discretisation

The mesh size of the model is chosen to correspond to the size of the lamellae cells. Every single lamellae section with dimensions - 150 mm in length and 35 mm in height - is one finite element (see Figures 5.1, 5.4). Three-dimensional solid continuum elements with 20 nodes and quadratic interpolation functions are used. Three elements are used along the thickness of the plate.

5.6.2 Boundary conditions

The plate is simply supported (see Figure 5.15). That means that at the lateral edges of the plate, displacements of the nodes are only allowed perpendicular to the edges in the plate plane. In mechanical terms, this means:

$$\begin{array}{l} at\ surfaces:\ x = 0\ and\ x = b:\ u_2 = u_3 = 0 \\ at\ surfaces:\ z = 0\ and\ z = b:\ u_1 = u_2 = 0 \end{array} \quad . \tag{5.18}$$

5.6.3 Loading

A surface load perpendicular to the plate is applied to the top surface. The magnitude of this distributed load is $P = 0.1$ [N/mm^2] (see Figure 5.16).

5.6.4 Material behaviour

In the framework of the finite element calculations, two types of computations are performed. First of all the reference plate, where all of the material parameters for each cell are constant (see Subsection 5.3.3), is computed once elastic and once elastic-plastic. The second type of calculations is made by computing of one hundred random plates, where every single plate has different material parameters, that are randomly assigned to each cell of the plate (see Subsection 5.3.2). Also every single random plate is calculated twice: once elastic and once elastic-plastic.

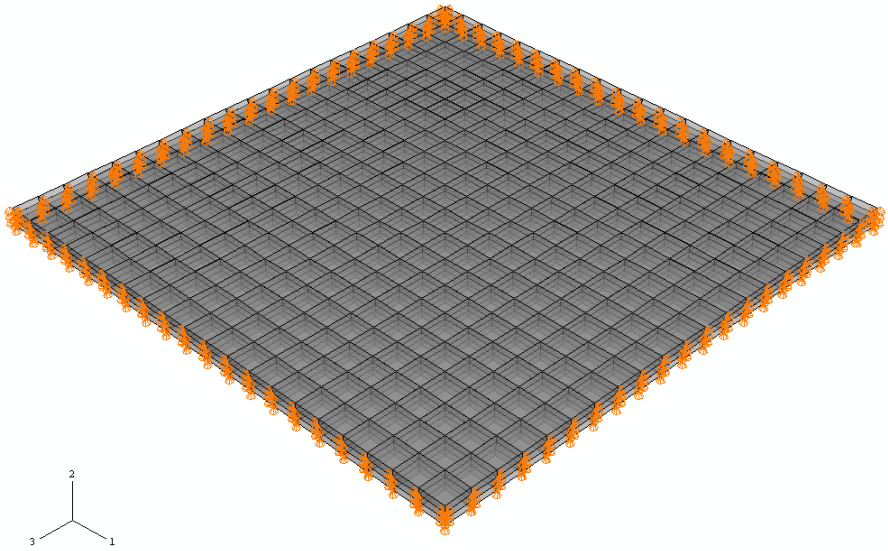

Figure 5.15: Boundary conditions

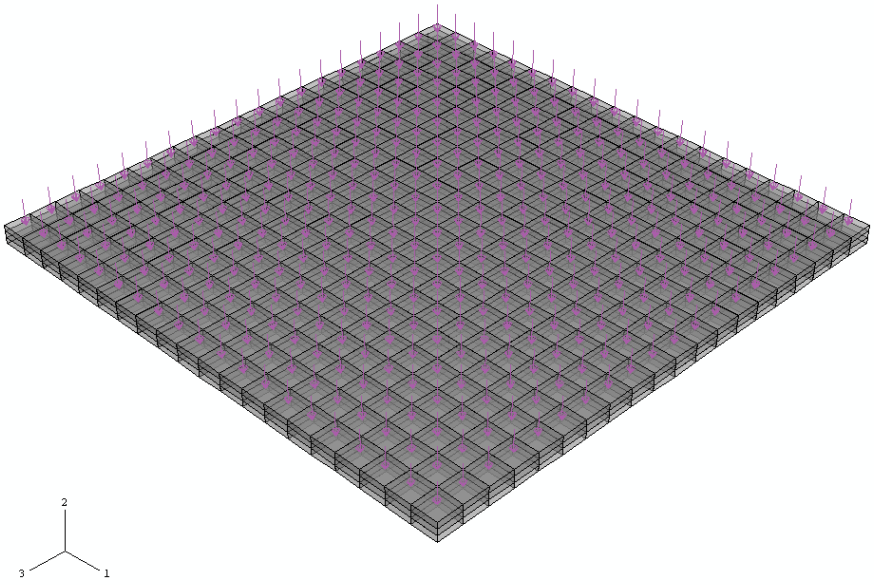

Figure 5.16: Loading - $P = 0.1$ [N/mm^2]

The elastic calculations are made according to the linear theory of elasticity (see Section 3.2), whereas the elastic-plastic calculations are performed using a Tsai-Wu failure criterion (see Section 3.3) and a Return-Mapping algorithm [28]. In the framework of the created model (MCLT) the following simplification is used: the plastic calculations are performed both for compression cells and tension cells i.e. also brittle failure modes are moduled as plastic.

Chapter 6

Results of the finite element simulations

The results of computations of CLT plates under bending load are presented. Firstly the reference plate is calculated. The elastic results of numerical computations are compared with corresponding analytical results. Also elastic-plastic computations are performed for the reference plate. Finally, results of elastic-plastic computations of the random plates are discussed.

6.1 The reference plate

In this section results of FEM calculations both elastic and plastic-elastic of the reference plate are presented. The elastic results of numerical calculations are compared with the analytical results to verify the correctness of the model. Using the results from elastic and elastic-plastic calculations the reference elastic limit is defined.

6.1.1 Elastic calculations

Results of numerical computations of the reference plate are compared with corresponding analytical calculation results [25], [26]. Presented in two cross-sections parallel to the plate boundaries through the midpoint, deflections u_2 in the mid-surface ($z = b/2$, $y = 0$ and $x = b/2$, $y = 0$), calculated with FEM (see Figure 6.1) are compared with the analytic results (see Figure 6.2).

According to the geometry and the orientation of cross-laminated timber (see Subsection 5.3.1), the main (longitudinal) direction of every layer is rotated by 90 degrees about an axis 2 against the next layer. Considering the orthotropic nature of wood, which is generally described in the framework of elasticity theory by means of the generalized Hooke's law (see Section 3.2),

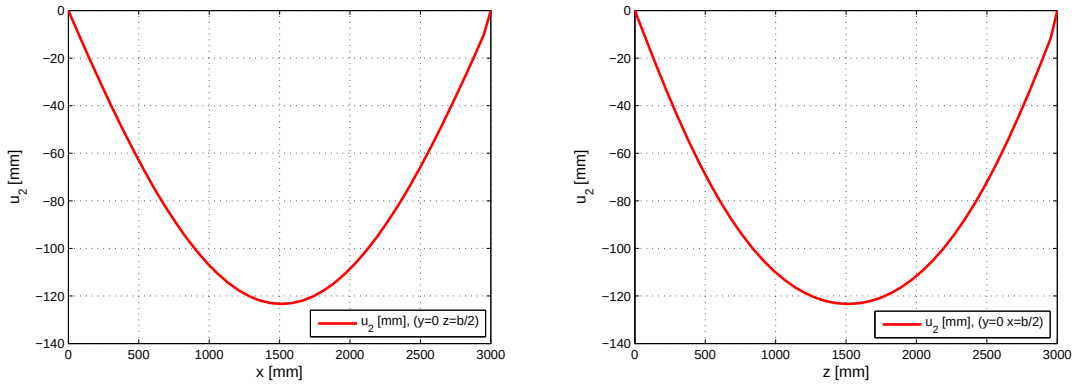

Figure 6.1: Plate deflections u_2 - FEM model

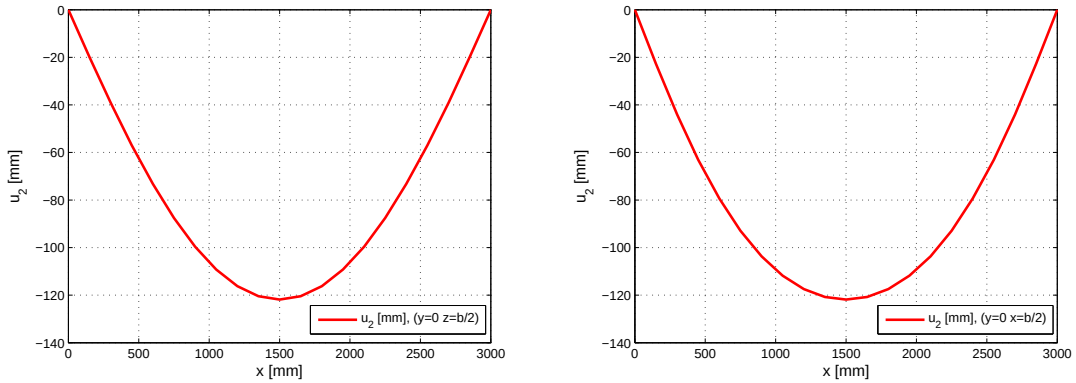

Figure 6.2: Plate deflections u_2 - analytic model

it is easy to understand the causes of stresses across the panel in thickness direction depicted in Figures 6.3 to 6.6. Both Figure, 6.3 showing stresses σ_{11} and σ_{33} obtained from numerical calculations using the MCLT, and 6.4, showing stresses σ_{11} and σ_{33} from analytic calculations, confirm the suitability of the model. The stresses are presented in the middle of the plate through the height ($x = b/2$, $z = b/2$). In each figure the central symmetry and the lamination of the plate can be observed. This is interpreted by the cross-laminated character of the plate, where the uneven layers, in which the longitudinal direction parallel to axis 1, show stiffer character along the global axis 1, while the even layers in which the longitudinal direction is oriented in parallel to axis 3, show stiffer character along global axis 3.

Considering the shear stresses (σ_{12}, σ_{23}) depicted in Figures 6.5 and 6.6 the symmetry of stresses along the mid-height of the plate is obvious. The shear stresses σ_{12} are presented in the middle of the edge of the plate, parallel to axis 3, through the height ($x = 0$, $z = b/2$), whereas the shear stresses σ_{23} are presented in the middle of the edge of the plate, parallel to axis 1, through the height ($x = b/2$, $z = 0$). Also here (in Figures 6.5 and 6.6), the lamination of the plate is visible: The upper and the lower layer have a similar stress values, whereas the middle layer behaves stay independently. All shear stresses show symmetry in the middle of the height of the plate. Comparing the analytically calculated shear stresses in Figure 6.6 with the

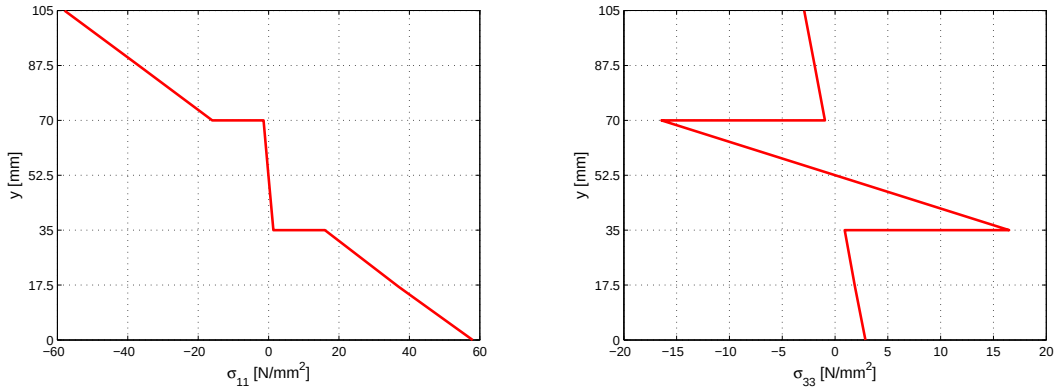

Figure 6.3: Course of tresses σ_{11}, σ_{33} through the plate thickness at $x = b/2$, $z = b/2$ - FEM model

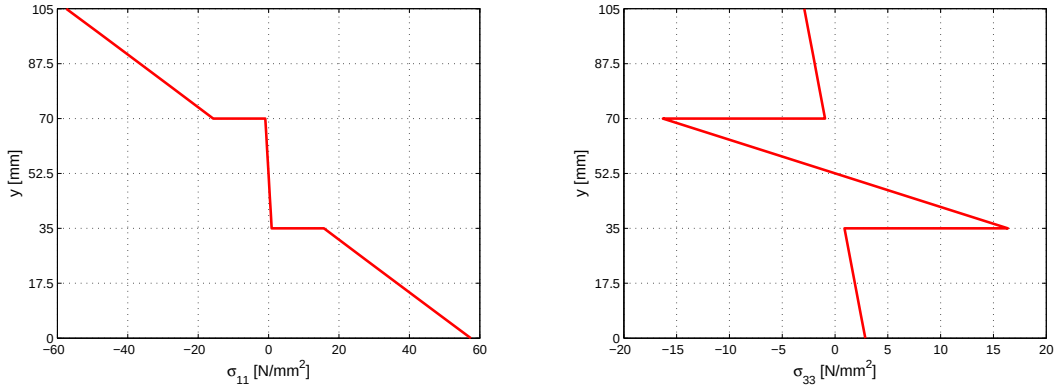

Figure 6.4: Course of stresses σ_{11}, σ_{33} through the plate thickness at $x = b/2$, $z = b/2$ - analytic model

numerically computed ones (Figure 6.5) confirms the suitability of the model.

The corresponding shear strains ϵ_{12} and ϵ_{23} are presented in the Figures 6.7 and 6.8. Both the analytic results (Figure 6.8) and the numerical ones (Figure 6.7), which are in general quite similar, show symmetry in the middle of the height of the plate also the lamination of the plate is clearly visible.

Figure 6.9 presents deflections in the middle of the plate ($x = b/2$, $z = b/2$, $y = h$) versus increasing loading. The linear dependence of deflections on load, within the elastic calculations is shown.

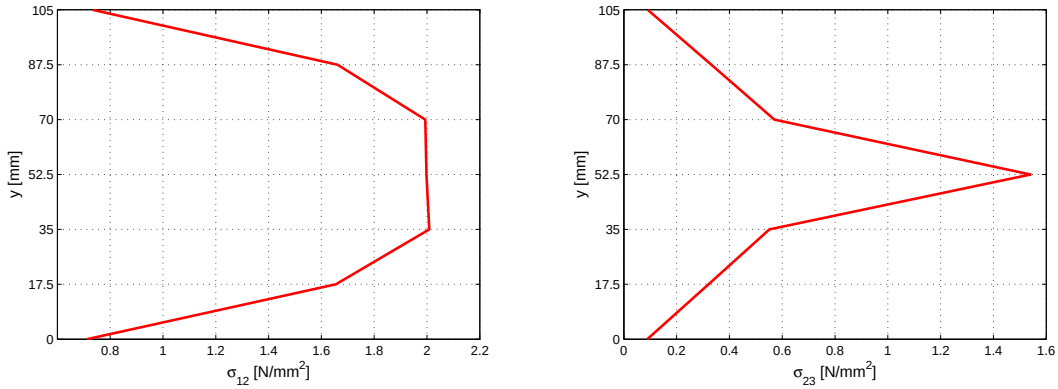

Figure 6.5: Course of shear stresses σ_{12} through the plate thickness at $x = 0$, $z = b/2$, and σ_{23} at $x = b/2$, $z = 0$ - FEM model

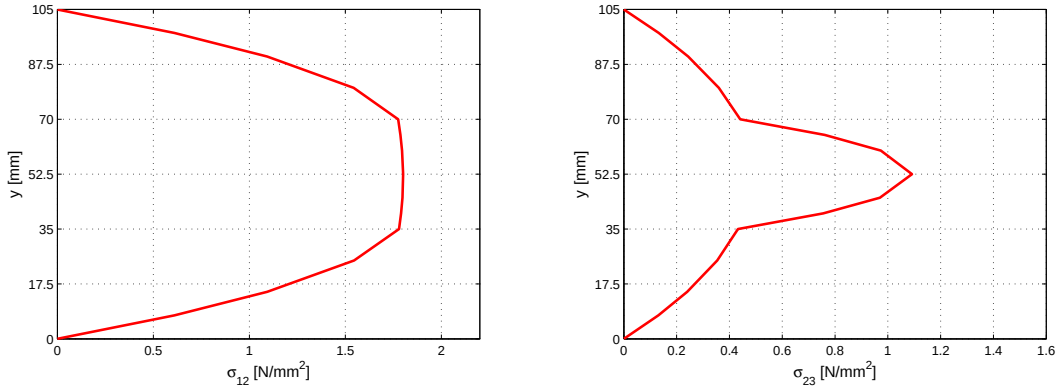

Figure 6.6: Course of shear stresses σ_{12} through the plate thickness at $x = 0$, $z = b/2$, and σ_{23} at $x = b/2$, $z = 0$ - analytic model

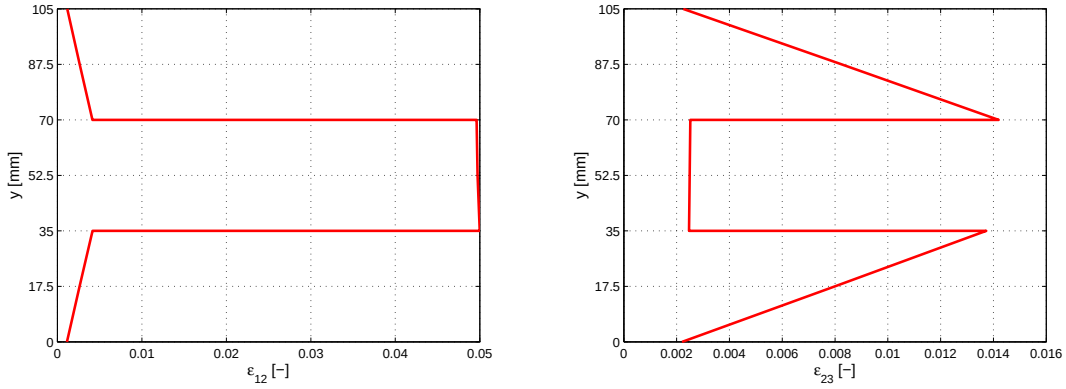

Figure 6.7: Course of shear strains ϵ_{12} through the plate thickness at $x = 0$, $z = b/2$, and ϵ_{23} at $x = b/2$, $z = 0$ - FEM model

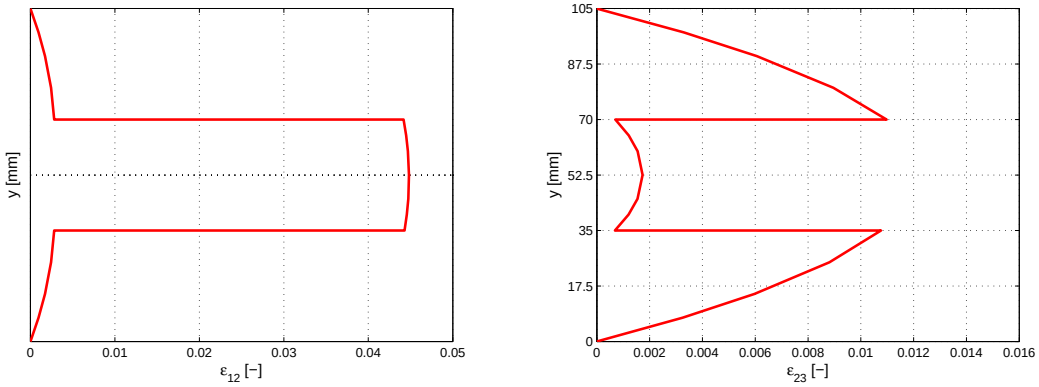

Figure 6.8: Course of shear strains ϵ_{12} through the plate thickness at $x = 0$, $z = b/2$, and ϵ_{23} at $x = b/2$, $z = 0$ - analytic model

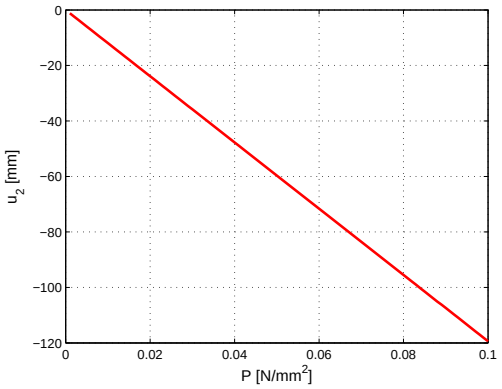

Figure 6.9: Deflection u_2 versus loading ($x = b/2$, $z = b/2$, $y = h$)

Figures 6.10 and 6.11 show the distributions of the stress components σ_{11} and σ_{33} in two perpendicular cross-sections through the plate mid-point parallel to the plate borders. Because of the cross-lamination geometry of the timber, the higher values of stresses are visible in stiffer layers (outer layers in Figure 6.10; middle layer in Figure 6.11).

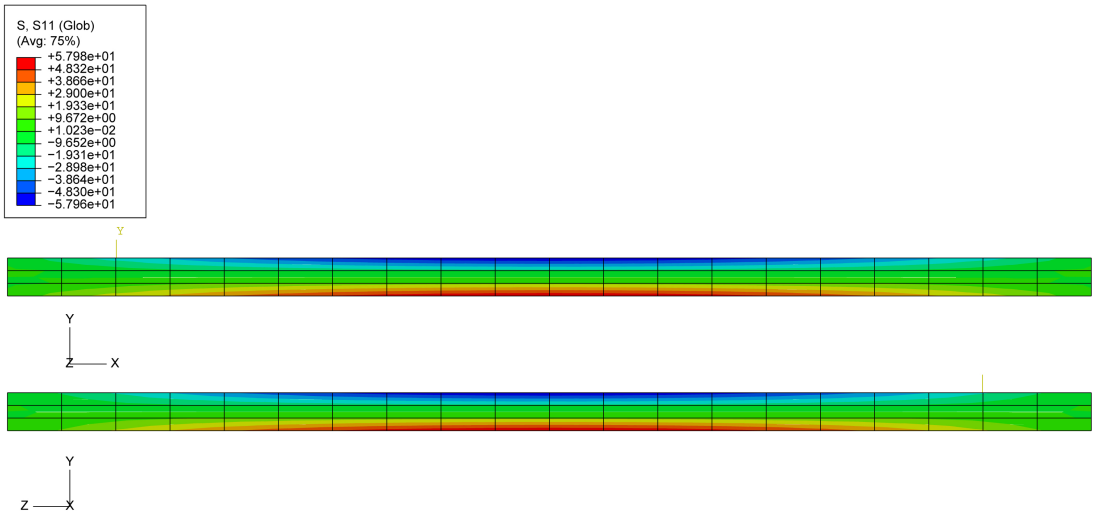

Figure 6.10: Distribution of σ_{11} [N/mm^2] in two cross-sections of plate: parallel to $z = b/2$ and parallel to $x = b/2$, respectively

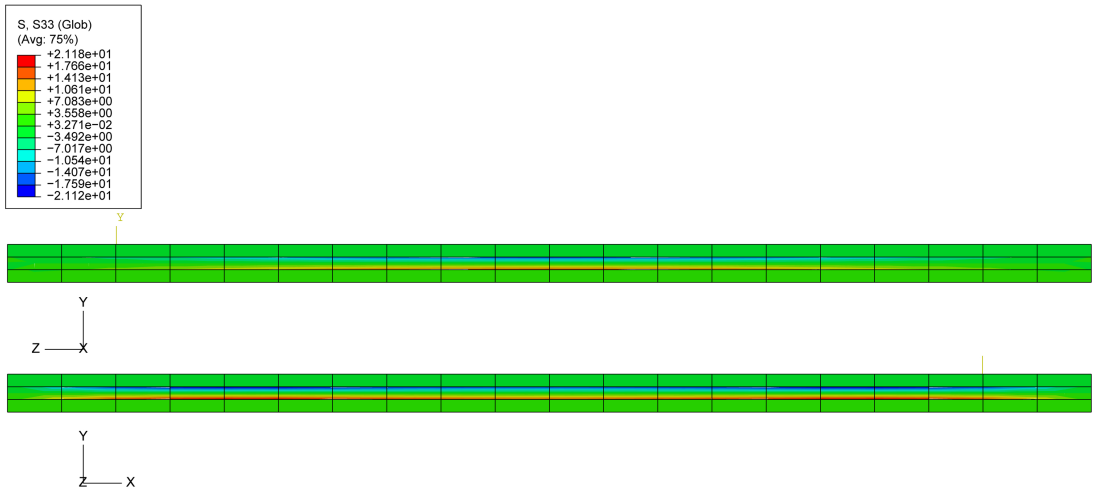

Figure 6.11: Distribution of σ_{33} [N/mm^2] in two cross-sections of plate: parallel to $z = b/2$ and parallel to $x = b/2$, respectively

The symmetric distribution of the stress component σ_{11} at the top surface of the plate is depicted in Figure 6.12. The component σ_{33} assumes a constant value of 0.1 N/mm^2 there corresponding to the applied surface load. As it was expected for the reference plate, the highest value of stresses σ_{11} are reached in the centre.

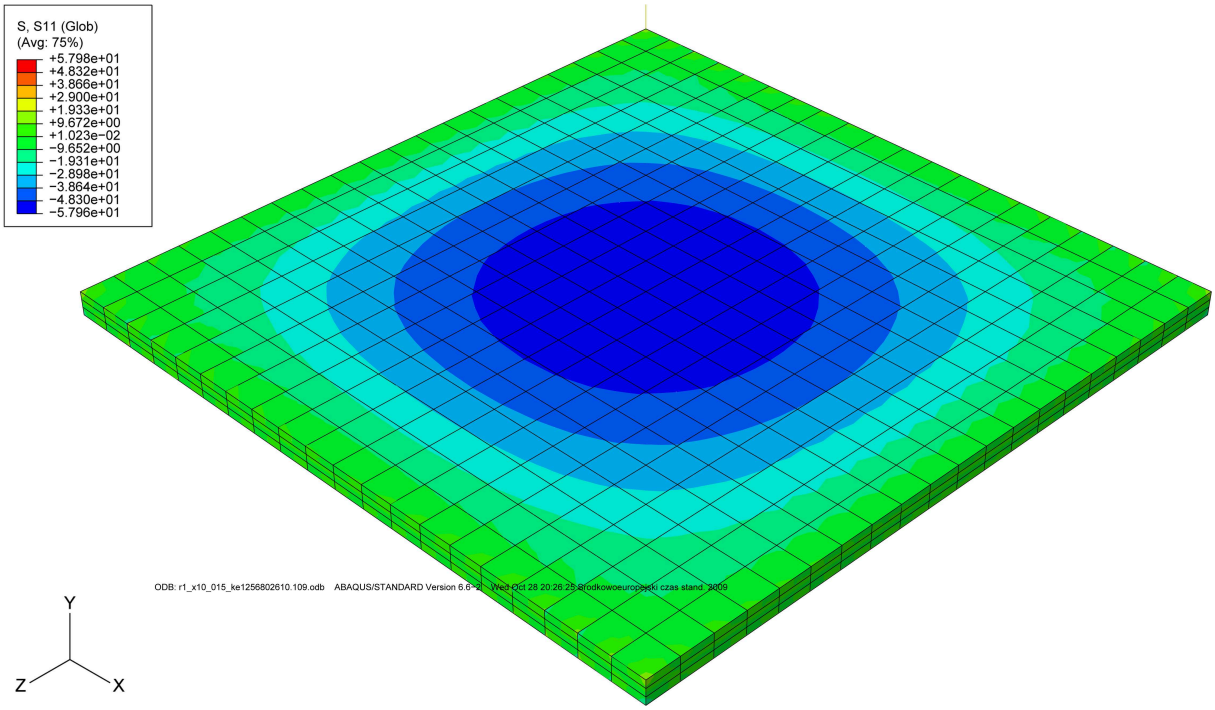

Figure 6.12: Distribution of stress components σ_{11} [N/mm^2] at the top surface

Shear stress component σ_{12} are depicted in Figure 6.13 in the mid-surface of the plate. Highest values of stresses σ_{12} are found at the borders parallel to axis 3.

The distribution of the plate deflection u_2 at the top surface is depicted in Figure 6.14. According to the boundary conditions and to the constant surface loading, the highest value of deflection is observed in the midpoint of the top surface.

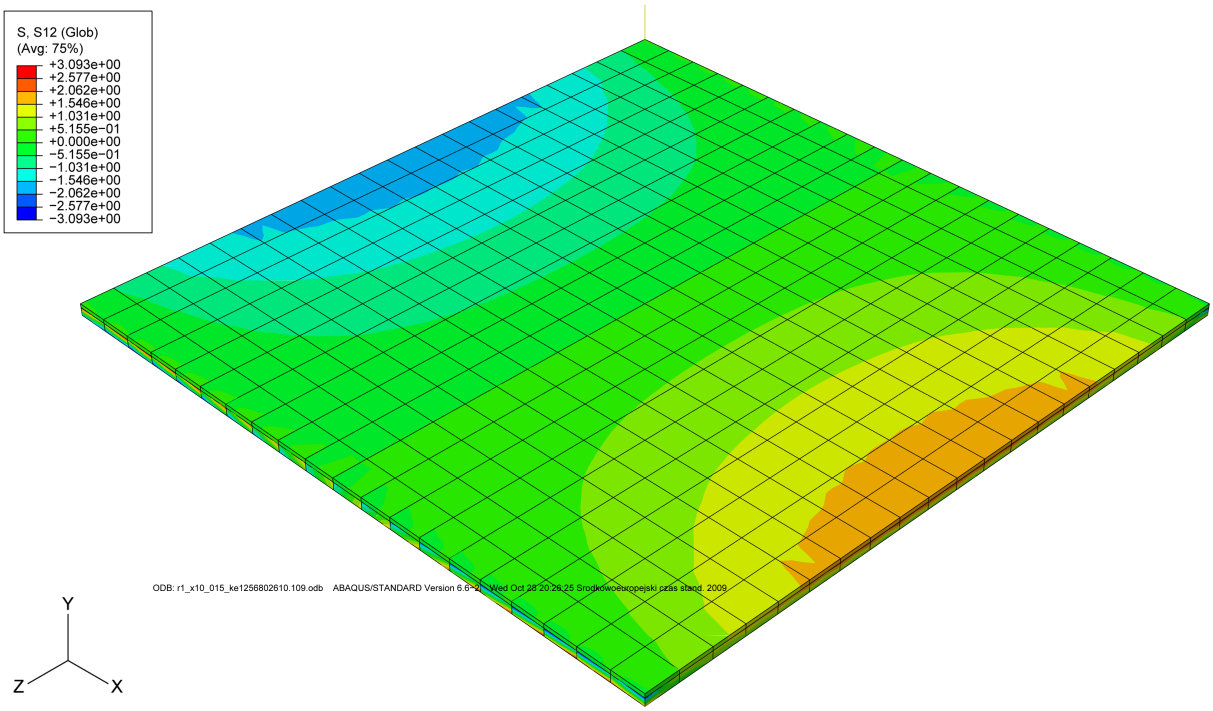

Figure 6.13: Distribution of stress components σ_{12} [N/mm^2] in the mid-surface

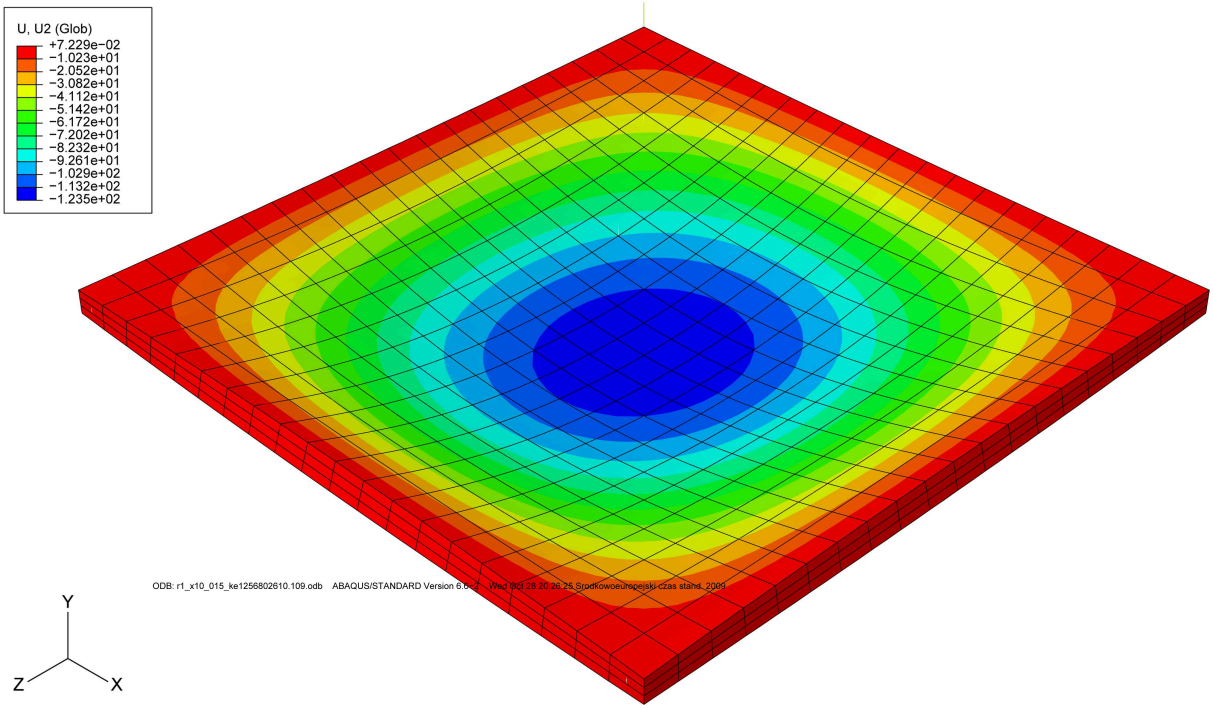

Figure 6.14: Distribution of deflections u_2 [mm] at the top surface

6.1.2 Elastic-plastic calculations

In this chapter the results of elastic-plastic computations of the reference plate are presented. All of the presented stresses are computed for the loading $P = 0.1$ N/mm^2. Figure 6.15 presents the course of the normal stress components σ_{11} and σ_{33} in the middle of the plate through the height ($x = b/2$, $z = b/2$). Now the distributions are not symmetric to the mid-surface any more. Some parts show constant values of stresses, in consequence of yielding of these parts of the reference plate. Again the lamination of the plate is observable, which influences the changes of the slope of the stress curves depicted in Figure 6.15.

Also the shear stresses σ_{12}, σ_{23} obtained in plastic calculations are presented (see Figure 6.15). Analogous to the elastic calculations, the results of shear stresses for elastic-plastic computations are presented in two sections: σ_{12} in the middle of the edge of the plate parallel to axis 3 through the height ($x = 0$, $z = b/2$); σ_{23} in the middle of the edge of the plate parallel to axis 1 through the height ($x = b/2$, $z = 0$). Comparing the shear stresses obtained in the elastic calculations with the corresponding elastic-plastic calculation results show higher values of both shear stresses in elastic-plastic case. This is a consequence of the considerably increased deflections under elastic-plastic conditions. The course of deflection versus loading is presented in Figure 6.17. The deflection is calculated in the midpoint of the top surface of the plate ($x = b/2$, $z = b/2$, $y = h$). The very gentle bending of the deflection is starting at the load $P = 0.031$ N/mm^2. Although it is not very distinctly observable in Figure 6.17, the plasticisation of the plate is evolving from this point onwards.

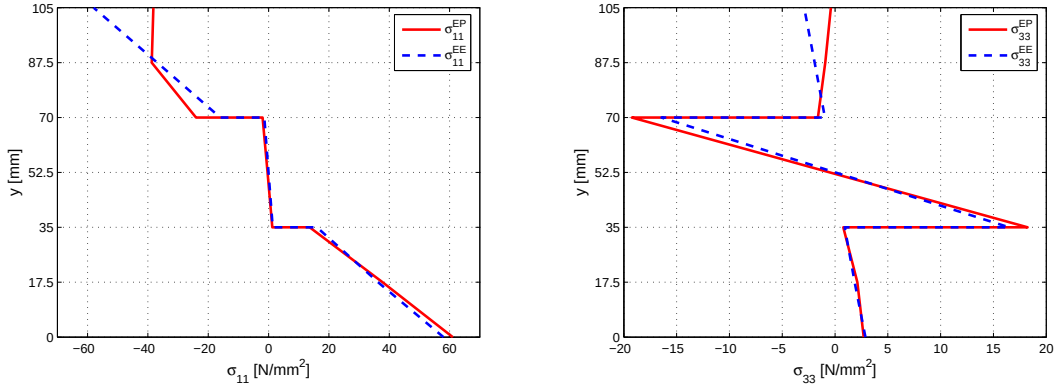

Figure 6.15: Course of stresses σ_{11}, σ_{33} through the plate thickness at $x = b/2$, $z = b/2$ - FEM model

The plasticisation of first elements of the reference plate mentioned before, which begins at a loading of $P = 0.031$N/mm^2, is illustrated in the Figure 6.18. Grey elements mark plasticized elements there. It is shown, that the plasticisation begins in the middle of the plate and at its edges.

Figures 6.19 and 6.20 show the distributions of the stress components σ_{11} and σ_{33} in two perpendicular cross-sections through the plate mid-point parallel to the plate borders. Also here,

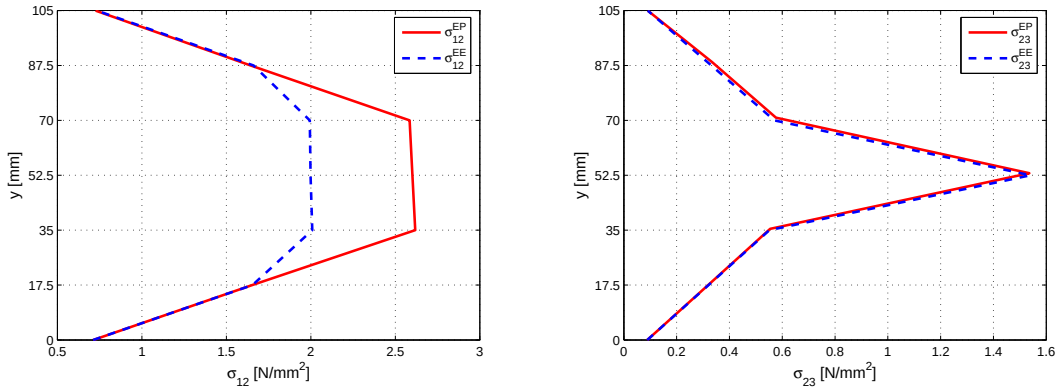

Figure 6.16: Course of shear stresses σ_{12} through the plate thickness at $x = 0$, $z = b/2$, and σ_{23} at $x = b/2$, $z = 0$ - FEM model

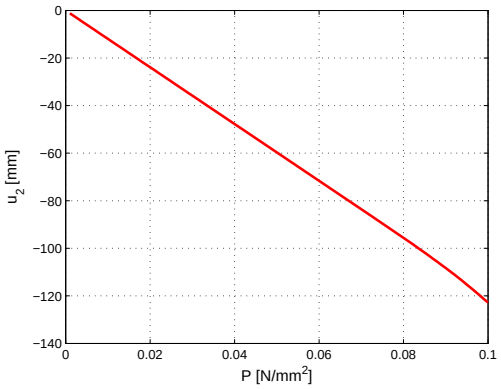

Figure 6.17: Deflection u_2 versus loading in the midpoint of the top surface ($x = b/2$, $z = b/2$, $y = h$)

because of the cross-lamination geometry of the timber, the higher values of stresses are visible in stiffer layers (outer layers in Figure 6.19; middle layer in Figure 6.20). Comparing Figures 6.10 and 6.11, presenting the distributions of the stress components for elastic calculations for elastic-plastic calculations respectively it is visible that lower values of stresses, which are more area splitted, determinate the elastic-plastic calculations.

The distribution of the stress component σ_{11} at the top surface of the plate is still symmetric as shown in Figure 6.21. The component σ_{33} again assumes a constant value of 0.1 N/mm^2 there corresponding to the applied surface load. Also for elastic-plastic computations, the highest value of stresses σ_{11} occur centrally. Stresses σ_{11} reach lower values in elastic-plastic calculations than in elastic computations, but large regions of the plate reach the maximum stress level (see Figure 6.21).

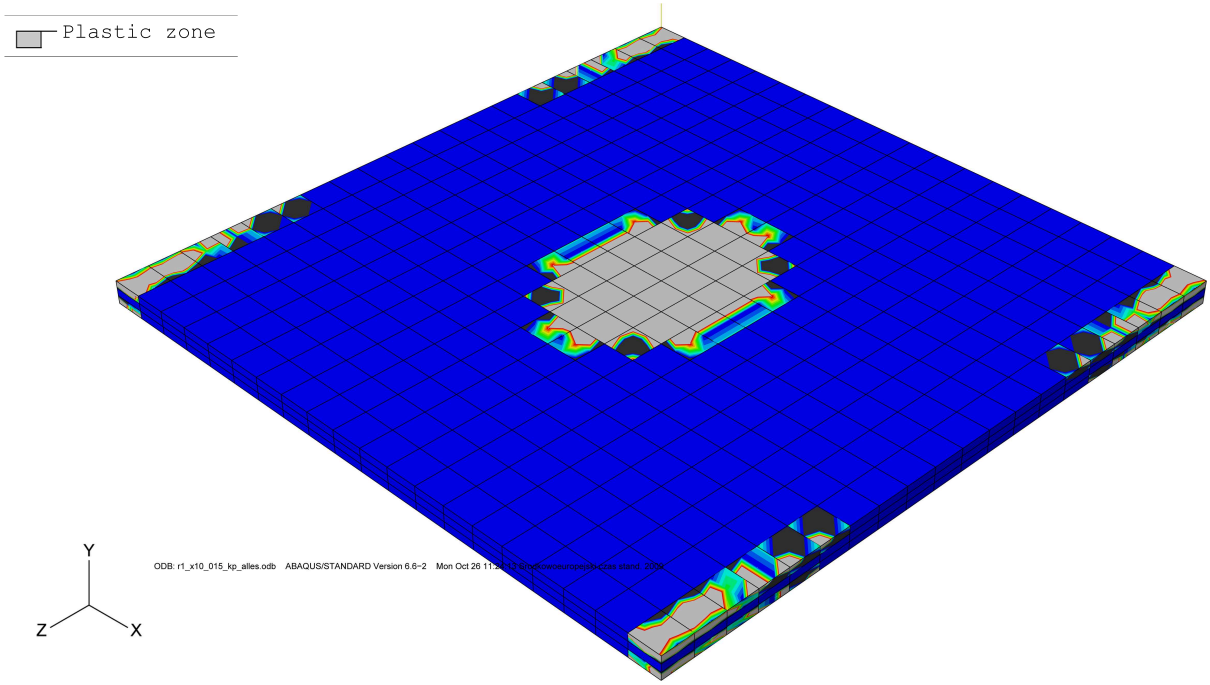

Figure 6.18: Beginning of the plasticisation of the reference plate - Tsai-Wu parameters

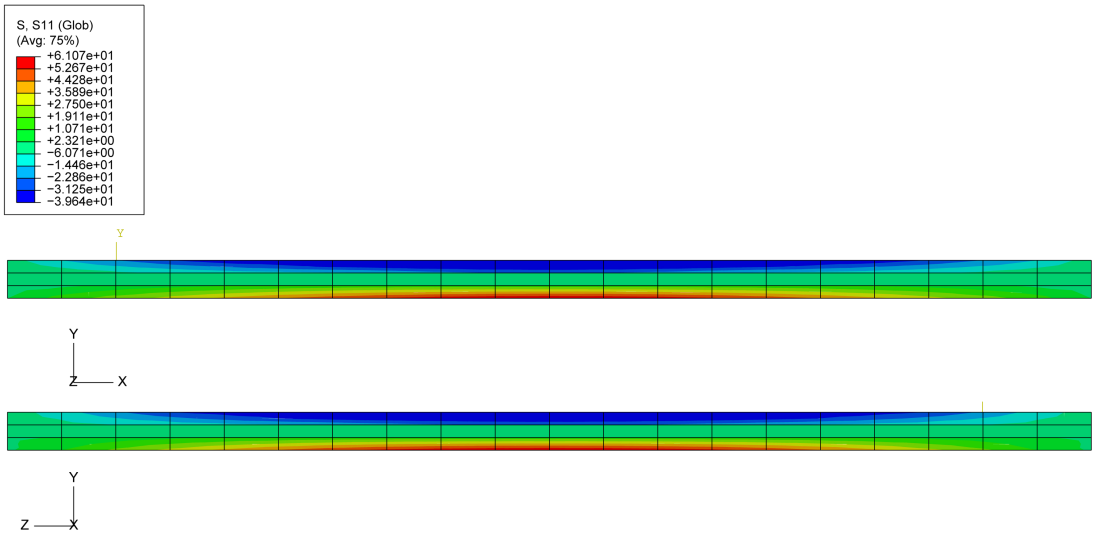

Figure 6.19: Distribution of σ_{11} [N/mm^2] in two cross-sections of the plate: parallel to $z = b/2$ and parallel to $x = b/2$, respectively

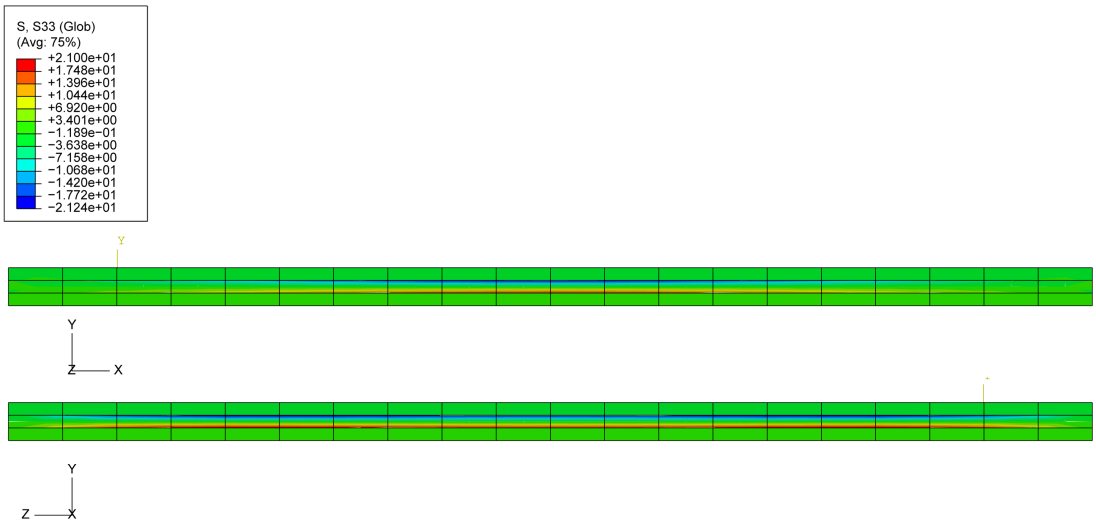

Figure 6.20: Distribution of σ_{33} [N/mm^2] in two cross-sections of the plate: parallel to $z = b/2$ and parallel to $x = b/2$, respectively

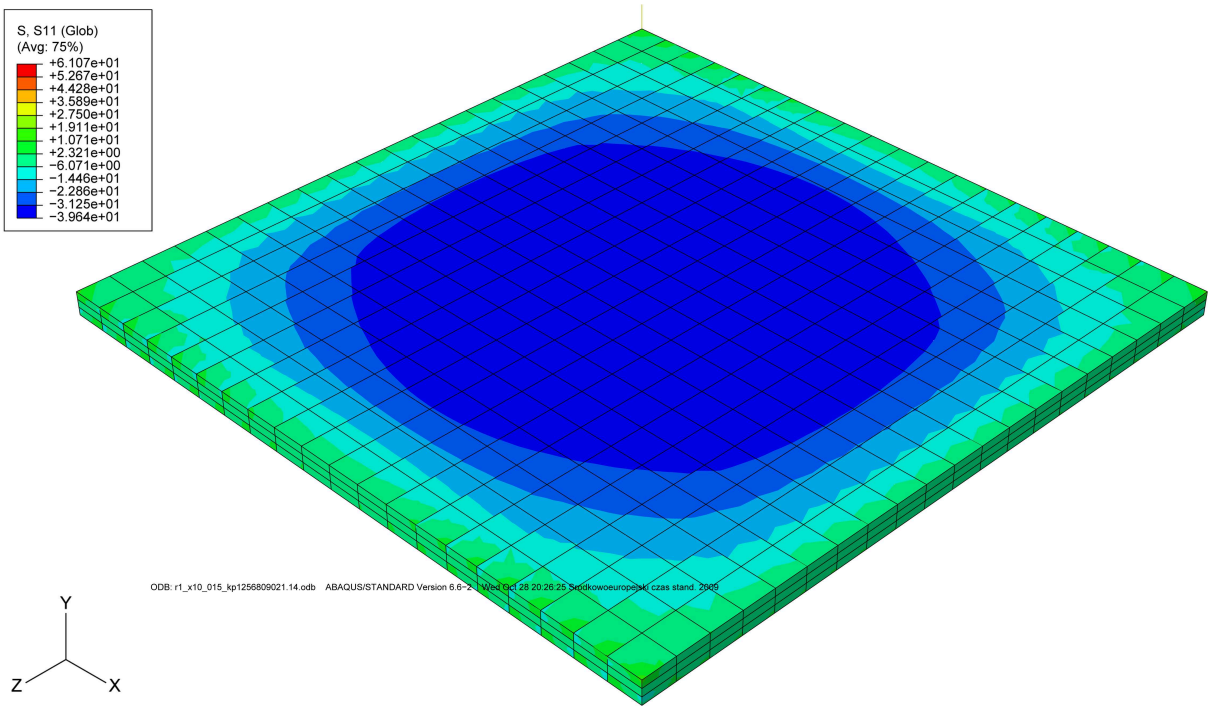

Figure 6.21: Distribution of stress component σ_{11} [N/mm^2] at the top surface

6.1.3 Elastic limit for reference plate

The relations between deflection and increasing loading $u(P_i)_2^{EE}$ for elastic calculations and $u(P_i)_2^{EP}$ for elastic-plastic are evaluated in the middle of the plate at the top surface ($x = b/2$, $z = b/2$, $y = h$). An apparent elastic limit is calculated as the highest load at which both calculations yield equal results, i.e. at which

$$\frac{u(P_i)_2^{EE}}{u(P_i)_2^{EP}} = 1 \; . \tag{6.1}$$

The elastic limit of the load is equal to $P = 0.031$ [N/mm^2] for the reference plate at an elastic limit deflection equal to $u_2 = 38.25$ [mm] (see Figure 6.22).

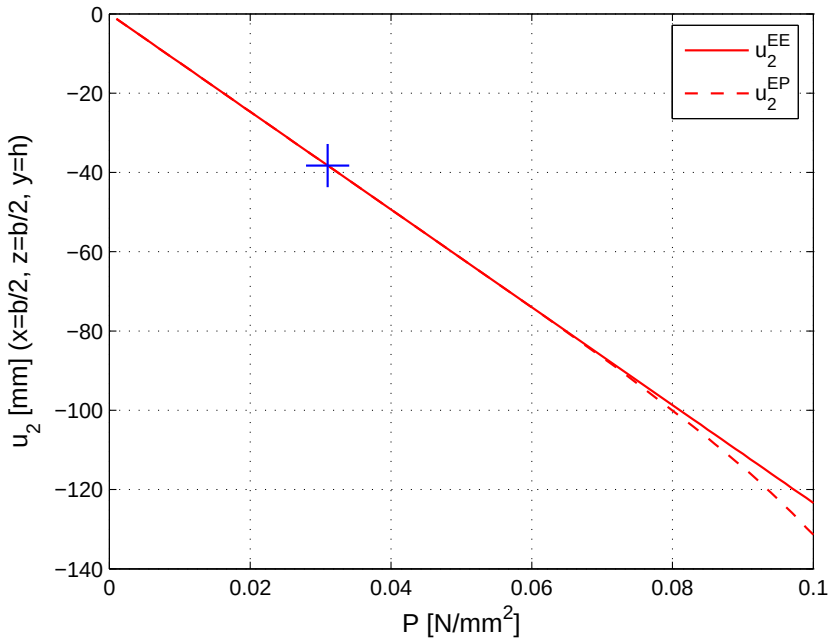

Figure 6.22: Deflections $u(P_i)_2^{EE}$ and $u(P_i)_2^{EP}$ versus loading in the mid-point of the top surface ($x = b/2$, $z = b/2$, $y = h$) - elastic limit (marked by +)

6.2 The random plates

In this section the results of FEM calculations of the random plates are presented. In contrast to the reference plate the random plate is randomly generated, and all of the material parameters are different for each cell of the plate (see Subsection 5.6.4). Hence, no symmetry and no regularity is expected in the presented results.

Numerical computations are performed for 100 random plates. The loading is $P = 0.1$ [N/mm^2].

For one example random plate, where the elastic limit is reached at a load $P = 0.0445$ [N/mm^2] and a deflection $u_2 = 55.15$ [mm], the distributions of Tsai-Wu parameters and of stress components σ_{11} and σ_{12} are presented. In particular, Figure 6.23 shows the Tsai-Wu parameter map for the top surface of the plate. The plasticisation of the first elements of the example random plate starts at the borders of the plate (see Figure 6.23).

The distribution of stress component σ_{11} in the middle part of the top surface of the random plate shows a large irregularity as depicted in Figure 6.24. The randomly assigned material parameters determinate the random distribution of this stress component, where no symmetry is visible. Also the distribution of the shear stress component $\sigma_1 2$ exhibits the irregular tendency and lack of symmetry in the mid-surface of the random plate. This is determinated by the varying material parameters in the random plate.

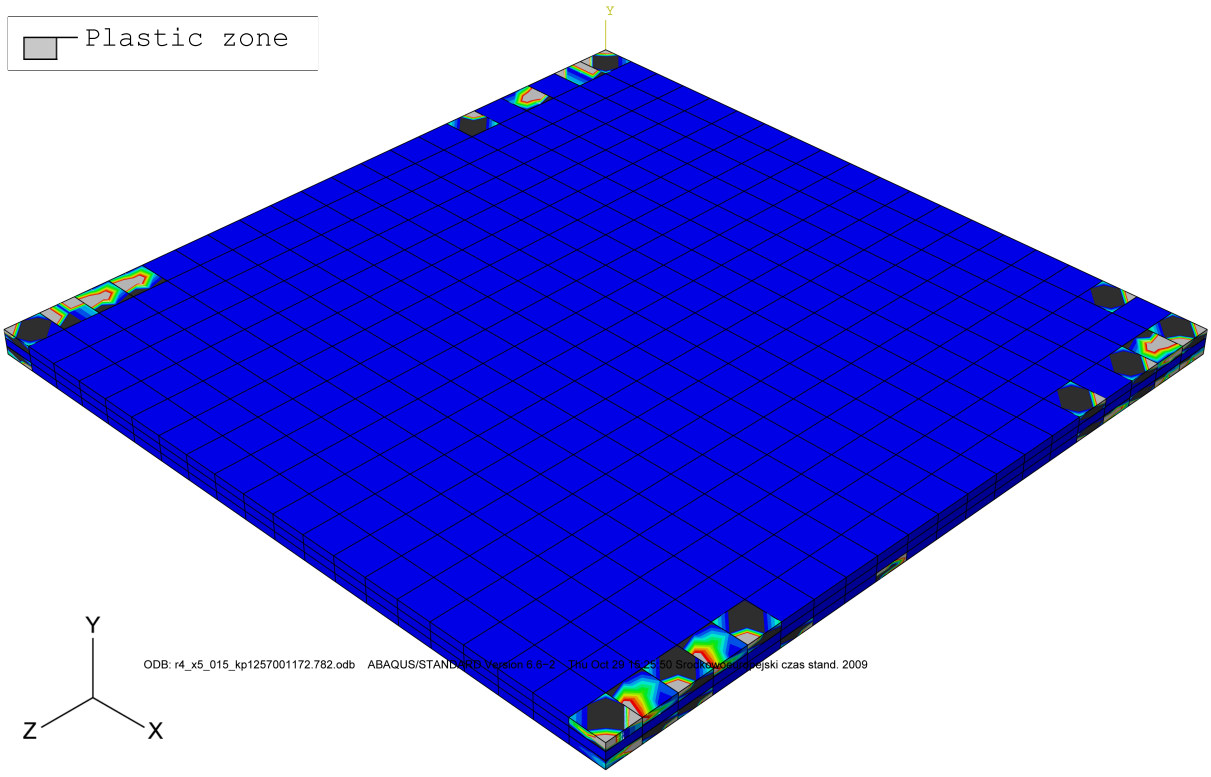

Figure 6.23: Beginning of the plasticisation of the random plate - Tsai-Wu parameters

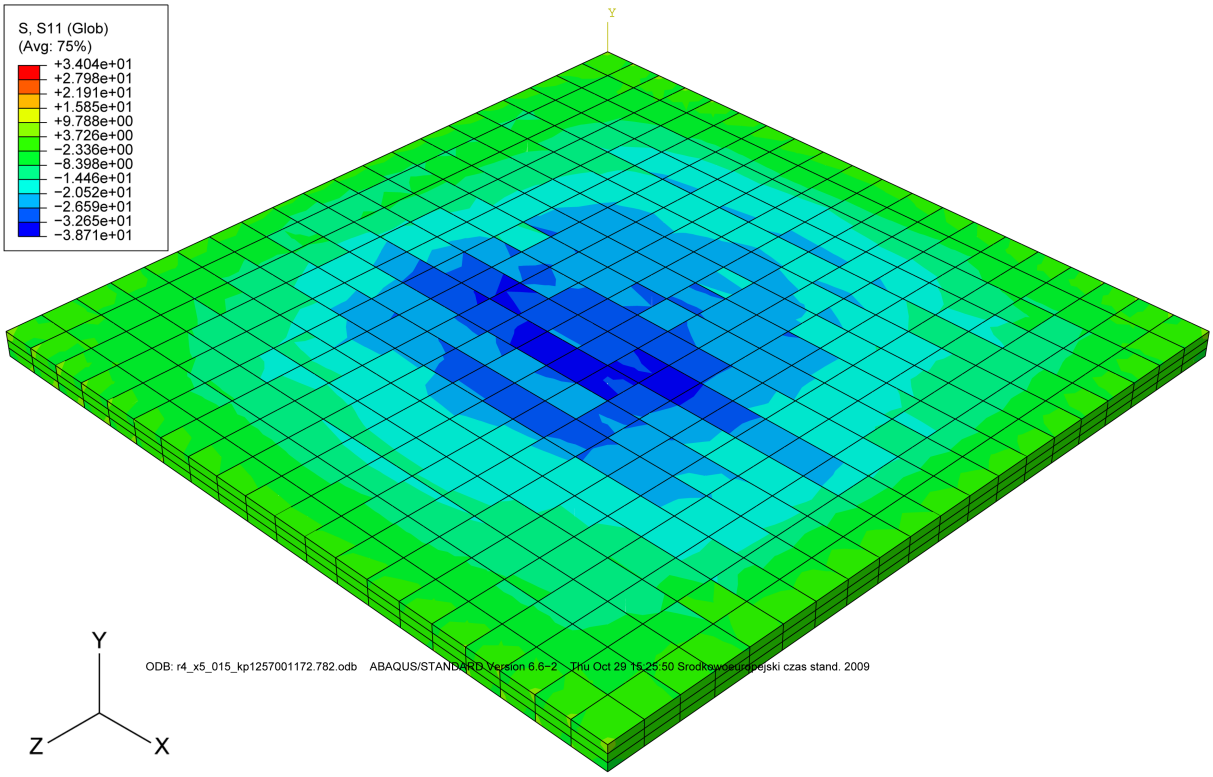

Figure 6.24: Distribution of stress component σ_{11} [N/mm^2] at the top surface

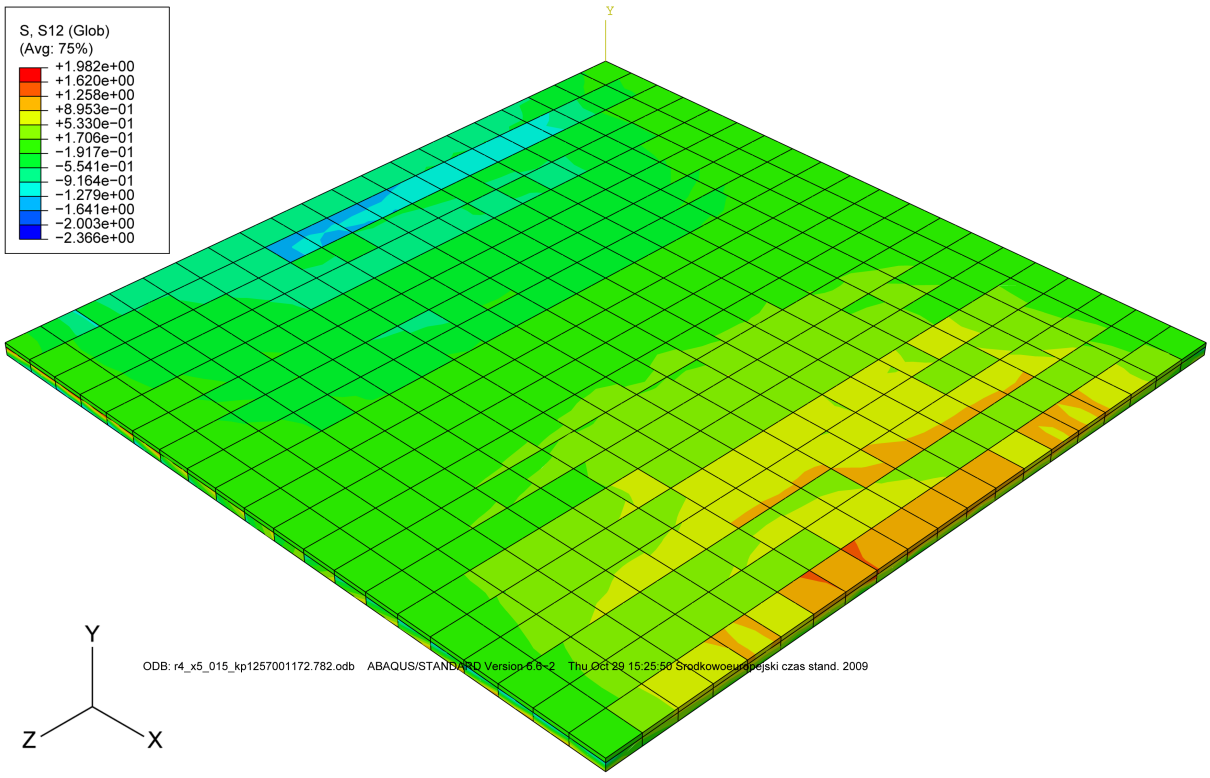

Figure 6.25: Distribution of stress component σ_{11} [N/mm^2] at the mid-surface

Next, three out of one hundred random plates with a different stiffness are chosen in order to show the variability of elastic limits (see Figures 6.26, to 6.28). These three plates are chosen by reason of different stiffnesses.

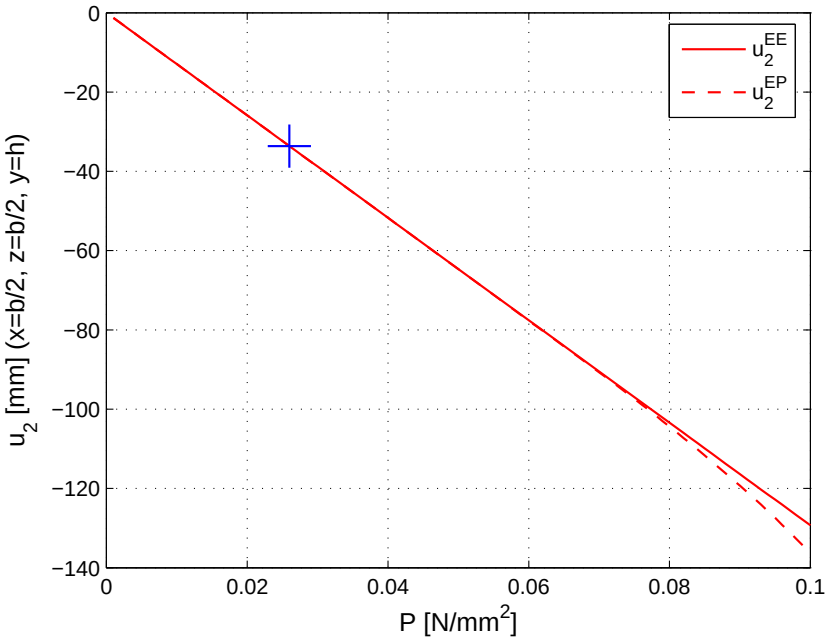

Figure 6.26: Deflections $u(P_i)_2^{EE}$ and $u(P_i)_2^{EP}$ versus loading at the midpoint of the top surface ($x = b/2$, $z = b/2$, $y = h$) - elastic limit for a random plate ($P = 0.007$ [N/mm^2], $u_2 = 9.052$ [mm])

One hundred random plates are simulated for determinating the distribution of elastic limits. Figure 6.29 presents the distribution of calculated deflections u_2 [mm], whereas Figure 6.30 show the corresponding distribution of elastic limit loads P [N/mm^2] at the midpoint of the top surface of the random plate ($x = b/2$, $y = h$, $z = b/2$). This deflection is used for evaluating the elastic limit.

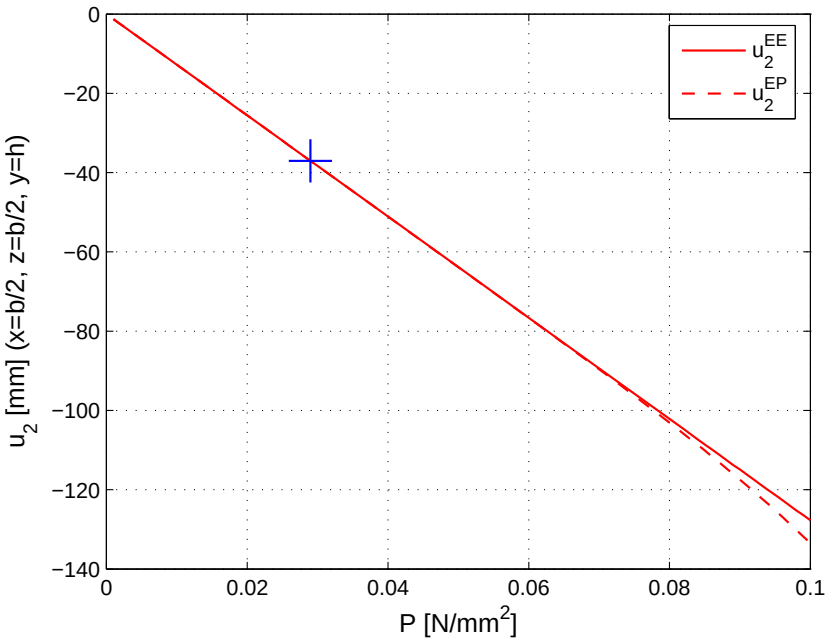

Figure 6.27: Deflections $u(P_i)_2^{EE}$ and $u(P_i)_2^{EP}$ versus loading at the midpoint of the top surface ($x = b/2$, $z = b/2$, $y = h$) - elastic limit for a random plate ($P = 0.036$ [N/mm^2], $u_2 = 45.98$ [mm])

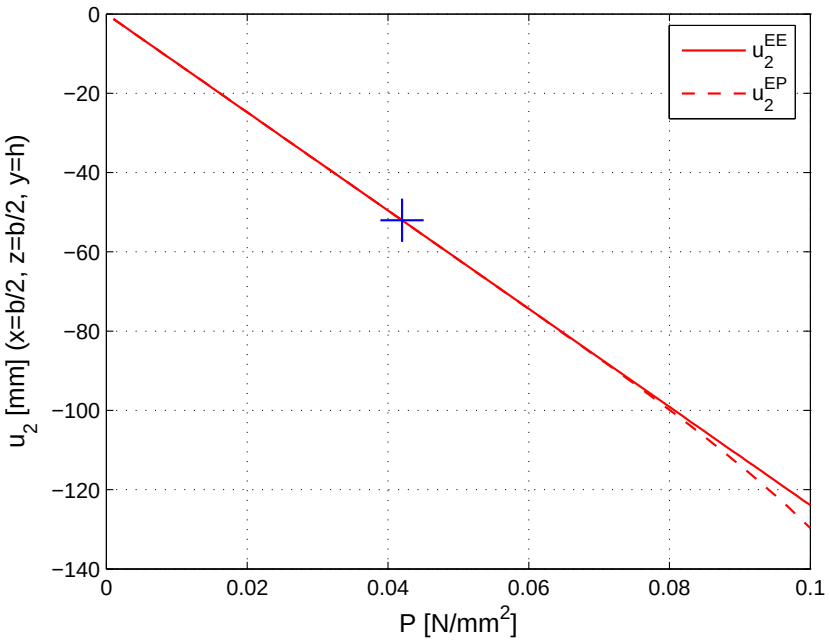

Figure 6.28: Deflections $u(P_i)_2^{EE}$ and $u(P_i)_2^{EP}$ versus loading at the midpoint of the top surface ($x = b/2$, $z = b/2$, $y = h$) - elastic limit for a random plate ($P = 0.0445$ [N/mm^2], $u_2 = 55.15$ [mm])

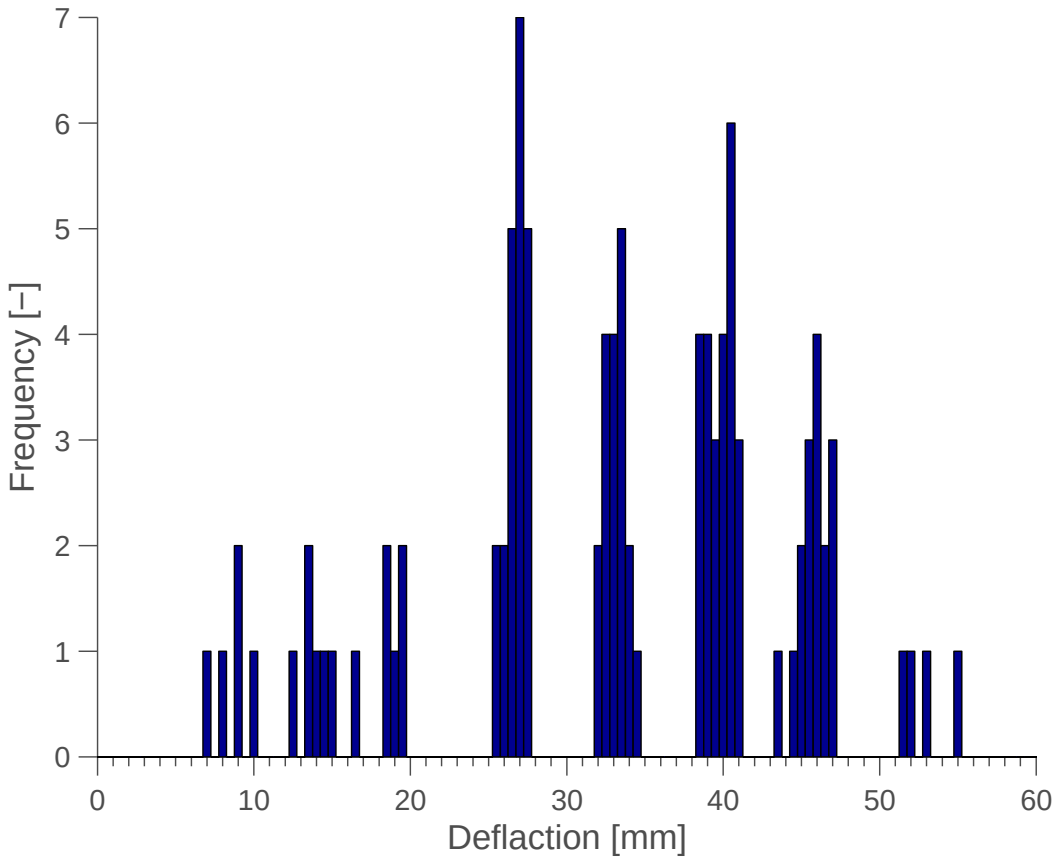

Figure 6.29: Histogram of frequency of deflections u_2 [mm] rounded to mm at the elastic limit of 100 random plates

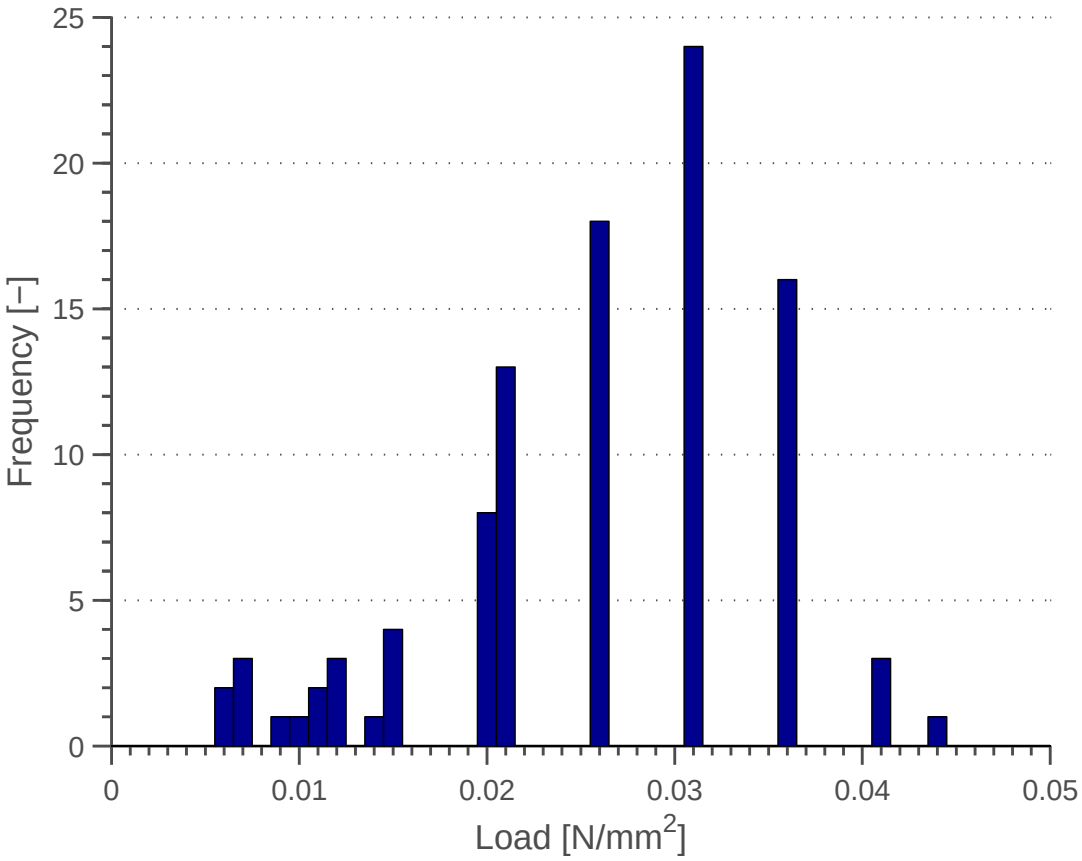

Figure 6.30: Histogram of frequency of loading P [N/mm^2] rounded to hundreds of [N/mm^2] at the elastic limit of 100 random plates

Chapter 7

Summary and conclusions

7.1 Summary

The main motivation for this thesis was to develop a simulation tool for investigation of the mechanical behaviour of cross-laminated timber and to apply it to studying the influence of varying mechanical characteristics of the individual lamellae on the overall plate behaviour. The developed Model for Cross-Laminated Timber (MCLT) is described. It is based on a two-dimensional model for glulam beams, the KAREM model, which is described in detail. The foundations of the MCLT, where variable lengths, densities, and knot content of the boards and a constant moisture content are taken into consideration, are depicted. Also some example calculations using MCLT are shown. Results of computations, using the MCLT in elastic range are compared with corresponding exact analytical results. The limit of elasticity for a reference plate with homogeneous mechanical properties and for one hundred random plates with varying mechanical properties randomly distributed using MCLT is estimated.

7.2 Conclusions

1. The variability of material parameters influences the stiffness and elastic limit of the cross-laminated timber.
2. The lamination of layers influences the distribution of stresses and strains.
3. The plasticization has effect on the distribution of displacements, stresses and strains.
4. The suitability of the MCLT for modelling the mechanical behaviour of CLT plates is shown.
5. The MCLT can be used for estimating the stiffness and the elastic limit load of the plate.

Chapter 8

Summary in Polish / Streszczenie

8.1 Rozdział 1 - Wstęp

Celem niniejszej pracy jest omówienie stworzonego modelu symulacyjnego płyty z drewna klejonego krzyżowo (MCLT - Model for Cross-Laminated Timber) oraz wpływu zmienności parametrów materiałowych na zachowanie się płyty podczas próby równomiernego zginania. Model MCLT powstał na bazie dwuwymiarowego modelu KAREM, symulującego belkę z drewna klejonego. Model MCLT zbudowany jest z dwóch programów: programu symulacyjnego oraz programu obliczeniowego. W ramach pierwszego programu odtworzono proces powstania tzw. nieskończenie długiej lameli, uwzględniając zmienność parametrów materiałowych drewna tj. gęstość, sękowatość, wilgotność oraz położenie połączeń klinowych. Program obliczeniowy oparty jest na metodzie elementów skończonych (MES). Za jego pomocą można wyznaczyć rozkład naprężeń, odkształceń oraz ugięć płyty. W ramach pracy przeprowadzono obliczenia sprężyste i sprężysto-plastyczne.

8.2 Rozdział 2 - Drewno klejone

W pierwszym podrozdziale 2.1 omówiono zalety i wady, a także zakres zastosowania drewna klejonego w konstrukcjach inżynierskich. Przedstawiony został również zarys procesu produkcji. Rycina 2.1 przedstawia przykładowe zastosowanie drewna klejonego w budownictwie.

W podrozdziale 2.2.1 wyszczególniono dwuwymiarowe obliczeniowe modele dla konstrukcji z drewna klejonego:

1. Model empiryczny Ik/Ig

2. Model bazujący na metodzie elementow skończonych (MES)

3. Metoda przekroju zastępczego

Model empiryczny uwzględnia przede wszystkim wpływ sękowatości wyrażony przez stosunek I_k/I_g (I_k - moment bezwładności przekroju poprzecznego sęków, I_g - moment bezwładności przekroju poprzecznego belki).

Model MES oparty jest na dwóch programach: symulacyjnym i obliczeniowym. Pierwszy program symuluje tzw. "nieskończenie długą lamelę" w oparciu o statystyczne rozkłady: gęstości, sękowatości, połączeń klinowych oraz stałej wilgotności drewna. W ramach drugiego programu przeprowadzane są obliczenia wytrzymałościowe. Model ten został wybrany, jako podstawa modelu trójwymiarowego MCLT, przedstawionego w niniejszej pracy

Metoda przekroju zastępczego bazuje na różnicy sztywności przekrojów EI.

W kolejnym podrozdziale 2.2.2 wyszczególniono dotychczasowe modele trójwymiarowe (3D):

1. Model bazujący na klasycznej teorii laminatów

2. Tzw. metoda gamma

3. Metoda bazująca na analogii ścinania

8.3 Rozdział 3 - Zarys teoretyczny

W podrozdziale 3.1 rycina 3.1 przedstawia zorientowanie wycinka drewna, gdzie L(2) - kierunek podłużny do włókien - R(3) kierunek radialny (prostopadły do przyrostu słojów) oraz T(1) - kierunek transwersalny (styczny do przyrostu słojów).

W podrozdziale 3.2 przedstawiono komplet równań teorii sprężystości w ujęciu ortotropowej natury drewna.

Kolejny podrozdział 3.3 przedstawia podstawy teoretyczne kryterium plastyczności Tsai-Wu, zdefiniowano tu parametry modelu. W obliczeniach użyto algorytmu powrotnego odwzorowania.

8.4 Rozdział 4 - KAREM - dwuwymiarowy model obliczeniowy drewna klejonego

W niniejszym rozdziale zaprezentowano model obliczeniowy, przedstawiony w 1985 roku przez Ehlbecka i in., dla belek z drewna klejonego. Model ten zbudowany jest z dwóch części, które zostały omówione w poniższych dwóch podrozdziałach.

Zadaniem programu symulacyjnego (omówionego w podrozdziale 4.2) jest odtworzyć proces produkcji belki z drewna klejonego. Program generuje "nieskończenie długą lamelę" (Ryc. 4.1), która składa się z listew połączonych ze sobą klinowo. Całkowita długość lameli jest zdeterminowana sumą długości poszczególnych listew. Każda listwa podzielona jest na 150 mm sekcje (komórki) - Ryc. 4.2. Zgodnie z normą DIN 4074 oraz regulacjami ECE rozmiar sekcji jest ściśle związany z definicją parametru sękowatości (KAR-value).

Używając statystycznych rozkładów parametrów materiałowych takich jak gęstość, sękowatość (KAR-value), wilgotność oraz połączenia klinowe każdej sekcji przyporządkowywana jest przypadkowa wartość tych parametrów (w oparciu o symulacje Monte Carlo). Ostatecznie celem programu symulacyjnego jest obliczenie wytrzymałości oraz sztywności dla każdej sekcji, za pomocą równań regresji.

W kolejnym podrozdziale 4.3 zostały omówione parametry materiałowe belki z drewna klejonego:

Geometria belki

Geometrię belki definiują dwa parametry: długość i wysokość. Warto wspomnieć, że szerokość zostaje pominięta z powodu podejścia dwuwymiarowego. Wysokość każdej listwy zawiera się w przedziale od 33 do 45 mm, która jest zdeterminowana przez dokładność równań regresji. Wysokość belki jest definiowana, jako wielokrotność wysokości poszczególnych listew.

Rozkład połączeń klinowych

Statystyczny rozkład połączeń klinowych jest sumą dwóch rozkładów normalnych będących wynikiem eksperymentu. Gęstość rozkładu połączeń klinowych przedstawiono na rycinie 4.3.

Gęstość

Rozkład gęstości oparty jest na badaniach Glosa (Ryc. 4.4). Jest to rozkład normalny, gdzie wszystkim sekcjom należącym do jednej listwy przyporządkowuje się tą samą wartość z rozkładu gęstości.

Sękowatość (KAR-value)

Wartość KAR definiuje się dla każdej sekcji, jako stosunek sumy powierzchni sęków w przekroju poprzecznym do pola powierzchni tego przekroju (Ryc. 4.5). W ramach programu symulacyjnego wartość KAR dla każdej sekcji jest przyporządkowywana z empirycznego rozkładu sękowatości - opracowanego przez Ehlbecka i in. dla klasy drewna II (Ryc. 4.6).

Wilgotność

> Nawiązując do Ehlbeck et al. dla całej belki przyporządkowana jest stała wilgotność $u = 12\%$.

Podrozdział 4.4 przedstawia równania regresji zaproponowane przez Ehlbecka i in. Równanie 4.1 przedstawia ogólną budowę użytych równań regresji, gdzie x_1, x_2 - niezależne zmienne wejściowe (takie jak gęstość, sękowatość) a_1,b_1,c_1 stałe wyznaczone eksperymentalnie, s_1 residuum analitycznej funkcji ln, które opisuje rozkład normalny, gdzie wartość średnia $\mu = 0$ oraz odchylenie standardowe $\sigma = 0$. Równania 4.2 definiują moduł sprężystości oraz wartości wytrzymałości na rozciąganie i ściskanie dla sekcji, które nie zawierają połączeń klinowych (ρ - gęstość, u - wilgotność, KAR - sękowatość), a równanie 4.3 odpowiednio dla sekcji zawierających połączenia klinowe.

W ramach programu obliczeniowego - przedstawionego w podrozdziale 4.5 - bazującego na metodzie elementów skończonych definiuje się: warunki brzegowe, obciążenia oraz rozmiar siatki elementów skończonych. Zakłada się, że każdy element siatki odpowiada swoimi wymiarami sekcji. Obliczenia odbywają się liniowo iteracyjnie, aż do momentu osiągnięcia wartości wytrzymałości w danej sekcji. Jeżeli osiągnięto wartość wytrzymałości na ściskanie, to w danej sekcji przyporządkowuje się tą wartość, jako stałe naprężenie do dalszych obliczeń. W przeciwnym razie, jeżeli osiągnięta została wartość wytrzymałości na rozciąganie, sekcja ta wyłączana jest z dalszych obliczeń otrzymując zerową wartość naprężeń.

8.5 Rozdział 5 - Model obliczeniowy płyt z drewna klejonego krzyżowo - MCLT

W prezentowanej pracy przedstawiony został trójwymiarowy model do obliczeń płyt z drewna klejonego krzyżowo. Model ten bazuje na założeniach modelu KAREM (program symulacyjny, program MES). W ramach omawianego modelu symuluje się kwadratową płytę. Program symulacyjny ma za zadanie wyznaczyć moduły Younga (E_L, E_R, E_T), moduły sprężystości przy ścinaniu (G_{LR}, G_{RT}, G_{TL}), stałe Poissona (ν_{LR}, ν_{RT}, ν_{TL}), a także wartości wytrzymałości (jednoosiowe wytrzymałości f_{y_L}, f_{y_R}, f_{y_T} dla rozciągania i ściskania oraz wartości wytrzymałości na ścinanie $f_{y_{LR}}$, $f_{y_{RT}}$, $f_{y_{TL}}$). Druga część modelu MCLT, oparta na MES, pozwala na przeprowadzenie obliczeń rozkładów naprężeń, odkształceń oraz ugięć płyty.

W ramach pracy zostały rozważone dwa rodzaje płyt: płyta referencyjna - w której każdej sekcji przypisana jest stała wartość parametrów materiałowych, a także brak połączeń klinowych, oraz płyta rzeczywista - gdzie każdej sekcji przyporządkowywane są losowo wybrane parametry materiałowe.
Płytę rzeczywistą, analogicznie do modelu KAREM, charakteryzują następujące parametry materiałowe:

Geometria płyty z drewna klejonego krzyżowo

Geometria płyty z drewna klejonego krzyżowo została zdefiniowana jak na rycinie 5.1. Płyta zbudowana jest z trzech warstw, gdzie lamele warstwy nieparzystej zorientowane są równolegle z osią 1, a parzyste równolegle z osią 3 (Ryc. 5.2, 5.3). Podobnie jak w modelu KAREM każda lamela zbudowana jest z listew, a każda z listew podzielona jest na sześcienne sekcje (Ryc. 5.4).

Parametry materiałowe płyty rzeczywistej

Zarówno wpływ połączeń klinowych, gęstości i wilgotności na parametry materiałowe w modelu MCLT jest analogiczny do modelu KAREM. Na użytek modelu aproksymowano rozkład sękowatości rozkładem Weibulla, gdzie każdej sekcji przyporządkowuje się losową wartość KAR (Ryc. 5.5).

W kolejnym podrozdziale zdefiniowane zostały równania regresji dla modelu MCLT.

Moduły sprężystości oraz współczynniki Poissona

Moduły sprężystości i współczynniki Poissona, uwzględniające wpływ gęstości i wilgotności, wyznaczone zostały za pomocą mikromechanicznego modelu (5.2). Powyższe równania zostały wyznaczone dla czystego drewna (bez wpływu sęków). Aby uwzględnić w równaniach regresji wpływ sęków, opracowano uproszczony trójwymiarowy model sęku (5.6) oraz wyznaczono współczynniki zmniejszające (5.3). Równania (5.5) oraz (5.7) przedstawiają moduły sprężystości i współczynniki Poissona z uwzględnieniem sękowatości. Warto wspomnieć, że dla płyty referencyjnej moduły sprężystości i współczynniki Poissona przyjmują wartości stałe (5.8).

Wartości wytrzymałości

Wstępnie zaczerpnięto z literatury referencyjne wartości wytrzymałości (5.9). Następnie używając modelu mikormechanicznego stworzono funkcje wpływu (5.7). Funkcje te, zależne od gęstości, mnoży się przez referencyjne wartości wytrzymałości (5.10). Ponownie otrzymane wartości obowiązują dla czystego drewna. Nawiązując do literatury i badań eksperymentalnych dla jednoosiowego ściskania wyznaczono funkcje redukujące wartości wytrzymałości dla czystego drewna, uwzględniające wpływ sęków (5.11, 5.12). Ponownie warto wspomnieć, ze wartości te są stałe dla płyty referencyjnej (5.13).

W rozdziale 5.5 przedstawiono studium wpływu wejściowych parametrów materiałowych na wartości modułów sprężystości, współczynników Poissona i wytrzymałości.

W pierwszym studium (podrozdział 5.5.1), gdzie parametry sprężystości uzależnione są od zmiennej gęstości, zauważalny jest wzrost wartości modułów sprężystości wraz ze wzrostem gęstości (Ryc. 5.9). Wartości współczynnika Poissona ν^k_{LT} oraz ν^k_{RT} maleją wraz ze wzrostem gęstości, podczas gdy wartości współczynnika Poissona ν^k_{RL} rosną wraz ze wzrostem gęstości (Ryc. 5.10). Wpływ wzrostu gęstości na wartości wytrzymałości jest analogiczny do zachowania się wartości modułu sprężystości - wraz ze wzrostem gęstości wzrasta wytrzymałość (Ryc. 5.11).

W drugim studium przedstawiono wpływ zmiany wartości KAR na wartości modułów sprężystości, współczynników Poissona oraz wytrzymałości. Jak widać na rycinie 5.12 wraz ze wzrostem wartości KAR wartości modułów sprężystości maleją. Wartości współczynnika Poissona ν^k_{LT} pozostają stałe, a wartości współczynników Poissona ν^k_{RL} i ν^k_{RT} rosną wraz ze wzrostem wartości KAR (Ryc. 5.13). Wszystkie wartości wytrzymałości maleją wraz ze wzrostem wartości KAR (Ryc. 5.14).

W kolejnym podrozdziale 5.6 przedstawiono drugą cześć modelu - program obliczeniowy. Do obliczeń metodą elementów skończonych użyto komercyjnego programu Abaqus 6.6.2. Rozmiar siatki elementów skończonych koresponduje z wielkością sekcji. Do obliczeń użyto elementów 20-węzłowych, stosując interpolację kwadratową. Płyta jest wolnopodparta, równania (5.18) opisują warunki brzegowe (Ryc. 5.15). Płytę obciążono stałym i równomiernie rozłożonym obciążeniem powierzchniowym o wartości $P = 0.1$ N/mm^2 (Ryc. 5.16). Każda płyta została obliczona dwukrotnie: sprężyście oraz plastycznie.

8.6 Rozdział 6 - Wyniki

W podrozdziale 6.1 zostały przedstawione oraz omówione wyniki otrzymane dla obliczeń płyty referencyjnej.

Obliczenia sprężyste

W niniejszym podrozdziale porównano wyniki obliczeń płyty referencyjnej wykonanych wyżej opisanym modelem (MCLT) z obliczeniami analitycznymi. Ryciny 6.2 do 6.13 przedstawiają kolejno ugięcie, rozkład naprężeń i odkształceń płyty referencyjnej w wybranych przekrojach.

Obliczenia sprężysto-plastyczne

Do obliczeń sprężysto-plastycznych użyto algorytmu powrotnego odwzorowania. Ryciny 6.15 do 6.21 przedstawiają rozkłady ugięć, naprężeń i odkształceń

w wybranych przekrojach płyty. Wskazano również początkowe uplastycznienie płyty referencyjnej przy obciążeniu $P = 0.031$ N/mm^2 (Ryc. 6.18).

Granica sprężysto-plastyczna

W ramach pracy zdefiniowano granicę sprężysto-plastyczną zgodnie z równaniem (6.1), gdzie $u(P_i)_2^{EE}$ dla obliczeń sprężystych, $u(P_i)_2^{EP}$ dla obliczeń sprężysto-plastycznych. W wyniku porównania maksymalnego ugięcia płyty obliczanego sprężyście z ugięciem płyty wyznaczonym modelem sprężysto-plastycznym obliczono granicę sprężysto-plastyczną dla płyty referencyjnej (Ryc. 6.22).

W podrozdziale 6.2 zostały przedstawione oraz omówione wyniki otrzymane w obliczeniach płyty rzeczywistej.

Przedstawiono wyniki obliczeń stu płyt rzeczywistych. Spośród nich wybrano trzy płyty o różnej sztywności. Ryciny 6.26 do 6.28 przedstawiają granice sprężysto-plastyczne dla wybranych płyt. Dla jednej płyty rzeczywistej, (która osiąga granice sprężysto-plastyczną dla obciążenia równego $P = 0.0445$ N/mm^2 i ugięcia maksymalnego $u_2 = 55.15$ mm) przedstawiono rozkłady naprężeń (Ryc. 6.24, 6.25). Ryciny 6.29 oraz 6.30 prezentują statystyczny rozkład gęstości maksymalnego sprężystego ugięcia oraz maksymalnego sprężystego obciążenia dla stu przeprowadzonych symulacji.

8.7 Rozdział 7 - Podsumowanie i wnioski

W przedstawionej pracy zaprezentowano model do obliczania płyt z drewna klejonego krzyżowo (MCLT), a także wyniki obliczeń przeprowadzonych przy użyciu opisanego modelu. Potwierdzono poprawność modelu MCLT dla płyty referencyjnej za pomocą rozwiązań analitycznych. Na podstawie otrzymanych wyników sformułowano następujące wnioski:

1. Zmienność parametrów materiałowych wpływa na sztywność i granicę sprężysto-plastyczną płyty z drewna klejonego krzyżowo.
2. Laminacja warstw wpływa na rozkład naprężeń i odkształceń.
3. Uplastycznienie determinuje rozkład naprężeń i odkształceń.
4. Wykazano poprawność modelu MCLT w ramach obliczeń płyt z drewna klejonego krzyżowo.
5. Model MCLT może być wykorzystany do wyznaczania nośności i uplastycznienia płyt z drewna klejonego krzyżowo.

Bibliography

[1] D.A. Bender, F.E. Woeste, E.L. Schaffer, and C.M. Marx. Reliability formulation for the strength and fire endurance of glued-laminated beams. Research paper FPL 460, U.S. Dept. Agric., For. Prod. Lab., 1985.

[2] H.J. Blaß, J. Ehlbeck, R. Görlacher, and Hättich. Karlsruher Forschung im Ingenieurholzbau 1987. 1987.

[3] K.M. Brown and S.K. Suddarth. A glued-laminated beam analyzer for conventional or reliability based engineering design. Research bulletin no. 940, Wood Research Laboratory, Purdue University, 1977.

[4] A.G. Burk. Reliability models for finger joint strength and stiffness properties in douglas-fir visual laminating grades, 1988. M.S. Thesis, Agricultural Engineering Dept., Texas A&M University, College Station.

[5] A.G. Burk and D.A. Bender. Simulating finger joint performance based on localized constituent lumber properties. *Forest Products Journal*, 39(3):45–50, 1989.

[6] F. Colling. Bending strength of laminated timber beams in relation to size effect: Development of a statistical model. *Holz als Roh- und Werkstoff*, 48:269–273, 1990.

[7] F. Colling. Bending strength of laminated timber beams in relation to size effect: Influence of beam size and type of loading. *Holz als Roh- und Werkstoff*, 48:321–326, 1990.

[8] F. Colling. Bending strength of laminated timber beams in relation to size effect: Verification of the statistical model by tests. *Holz als Roh- und Werkstoff*, 48:391–395, 1990.

[9] J. Eberhardsteiner. *Mechanisches Verhalten von Fichtenholz: Experimentelle Bestimmung der biaxialen Festigkeitseigenschaften*. Springer Verlag, Wien, New York, 2002.

[10] J. Ehlbeck, F. Colling, and R. Görlacher. Influence of finger-jointed lamellae on the bending strength of gluelam beams: Development of a computer model. *Holz als Roh- und Werkstoff*, 43(8):333–337, 1985.

[11] J. Ehlbeck, F. Colling, and R. Görlacher. Influence of finger-jointed lamellae on the bending strength of gluelam beams: Input data for the computer model. *Holz als Roh- und Werkstoff*, 43(9):369–373, 1985.

[12] J. Ehlbeck, F. Colling, and R. Görlacher. Influence of finger-jointed lamellae on the bending strength of gluelam beams: Verification of the computer model by bending tests. *Holz als Roh- und Werkstoff*, 43(9):439–442, 1985.

[13] M. Fleischmann. *Numerische Berechnung vom Holzkonstruktionen unter Verwendung eines realitëtsnahen orthotropen elasto-plastischen Werkstoffmodells*. Doctoral thesis, Technische Universität Wien, Österreich, 2005.

[14] R.O. Foschi and J.D. Barrett. Glued-laminated beam strength: A model. *Journal of Structural Engineering (ASCE)*, 106(8):1735–1754, 1980.

[15] A.D. Freas and M.L. Selbo. Fabrication and design of glued laminated wood structural members. Technical bulletin no. 1069, U.S. Dept. Agric., For. Prod. Lab., 1954.

[16] P. Glos. Zur Bestimmung des Festigkeitsverhaltens von Brettschichtholz bei Druckbeanspruchung aus Werkstoff- und Einwirkungskenngrößen. Heft 35, Sonderforschungsbereich 96, München, 1987.

[17] R. Govindarajoo. *Simulation modeling and analyses of straight horizontally laminated glulam timber beams*. Doctoral Thesis, Purdue University West Lafayette, 1989.

[18] R. Keylwerth. Die anisotrope Elastizität des Holzes und der Lagenhölzer [The anisotropic elasticity of wood and laminated timber] (in German). *VDI-Forschungsheft*, 430, 1941.

[19] D.E. Kline, F.E. Woeste, and B.A. Bendtsen. Stochastic model for modulus of elasticity of lumber. *Wood and Fiber Science*, 18(2):228–238, 1986.

[20] F. Kollmann. *Technologie des Holzed und der Holzwerkstoffe*, volume 1. Springer-Verlag, Berlin, 2 edition, 1982.

[21] H. Kühne. Über den Einfluß von Wassergehalt, Raumgewicht, Faserstellung und Jahrringstellung auf die Festigkeit und Verformbarkeit schweizerischen Fichten-, Tannen-, Lärchen-, Rotbuchen- und Eichenholzes. 1955.

[22] H.J. Larsen. Strength of glued laminated beams. Part 2 (properties of glulam laminations). Report no. 8004, Institute of Building Technology and Structural Engineering, Aalborg University, DK, 1980.

[23] R.C. Moody. Design criteria for large structural glued-laminated timber beams using mixed species of visually graded lumber. Research paper FPL 236, U.S. Dept. Agric., For. Prod. Lab., 1974.

[24] R.C. Moody. Improved utilization of lumber in glued-laminated beams. Research paper FPL 292, U.S. Dept. Agric., For. Prod. Lab., 1977.

[25] N.J. Pagano. Exact solutions for composite laminates in cylindrical bending. *Composite Materials*, 3:398–411, 1969.

[26] N.J. Pagano. Exact solutions for rectangular bidirectional composites and sandwich plates. *Composite Materials*, 4:20–34, 1970.

[27] B.A. Richburg. Optimization of glued-laminated beam performance, 1988. Undergraduate Fellows Thesis, Agricultural Engineering Dept., Texas A&M University.

[28] J.C. Simo and T.J.R. Hughes. *Computational inelasticity*. Springer, Berlin, Germany, 1998.

[29] S.E. Taylor. *Modeling spatially correlated localized lumber properties*. Dissertation, Agricultural Engineering Dept., Texas A&M University, 1988.

[30] T.R.C. Wilson and W.S. Cottingham. Tests of glued-laminated wood beams and columns and development of principle of design. Report no. r1687, U.S. Dept. Agric., For. Prod. Lab., 1947.